TUDelft

Delft University of Technology

Toward identifying the ASR-induced stresses from displacement measurements and crack observations—Demonstration on a beam bridge in Norway

Kongshaug, Simen Sørgaard; Hendriks, Max A.N.; Kanstad, Terje; Markeset, Gro

Important note
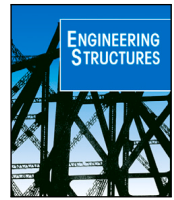To cite this publication, please use the final published version (if applicable).
Please check the document version above.

Check for updates

Toward identifying the ASR-induced stresses from displacement measurements and crack observations—Demonstration on a beam bridge in Norway

Simen Sørgaard Kongshaug [a,b,*], Max A.N. Hendriks [b,c], Terje Kanstad [b], Gro Markeset [a]

[a] Oslo Metropolitan University, Pilestredet 35, 0130 Oslo, Norway
[b] Norwegian University of Sciences and Technology, Richard Birkelandsvei 1A, 7034 Trondheim, Norway
[c] Delft University of Technology, Stevinweg 1, 2628 CN Delft, The Netherlands

ARTICLE INFO

ABSTRACT

Alkali–silica reaction (ASR) in concrete causes expansion and degradation of the material, which might give adverse structural consequences. From the structural engineer point view, the greatest concern is if ASR leads to loss of structural integrity. Two natural questions arise when assessing existing concrete structures affected by ASR: (1) how to calculate the ASR-induced stresses, and (2), when the ASR-induced stresses are calculated, what is the residual capacity when accounting for the material deterioration caused by ASR? This study aimed to contribute in answering the first question.

The ASR-induced stresses can be calculated in a structural analysis that includes a concrete material model that incorporates the effects of ASR on the material behaviour, i.e. expansion and material deterioration. Many such models exist. However, these models rely on predefined field variables, e.g. moisture and temperature, which are (generally speaking) unknowns for an existing structure. Consequently, structural analysis of ASR-affected concrete structures involves dealing with unknown field variables. From this background, we developed a material model and a suitable structural analysis method. The material model relies on only one predefined, howbeit unknown, field variable —the free ASR expansion. The structural analysis method is based on solving an inverse problem, which is to back-calculate the free ASR expansion field from a set of measured displacements.

The material model and the structural analysis method were applied in a structural analysis of an ordinary reinforced beam bridge in Norway. Then, the imposed deformations and stresses due to ASR were investigated to increase the understanding of the structural consequences of ASR in ordinary reinforced continuous beam bridges.

1. Introduction

The effects of alkali–silica reaction (ASR) in concrete are expansion and degradation of the material [1–4]. At the structural level, the most visible signs of ASR are surface cracks and displacements. For bridges, displacements may lead to a reduction of expansion joints and inclined columns (an angle to the vertical position) due to the elongation of bridge superstructure [5]. From the structural mechanical point of view, this concrete expansion can be considered and modelled as an imposed strain (additional strain), denoted ASR expansion. From other imposed strains, like thermal and shrinkage strain, we know that they cause stresses either if the imposed strain field is strain incompatible,[1] or if the resulting displacements are restrained by the displacement boundary conditions, where the latter only happens for statically indeterminate structures. In ASR-affected reinforced concrete (RC) structures, the ASR expansion field only applies to the concrete, and therefore, it is always strain incompatible as the embedded reinforcement is non-expanding. Consequently, tensile stresses develop in the reinforcement, and compressive stresses in the concrete, which is often referred to as the pre-stressing effect. Again, additional stresses occur if the imposed ASR expansion field leads to displacements that are restrained by the displacement boundary conditions, as in continuous beam bridges [6]. In this paper, the incompatibility of the ASR

---

* Corresponding author at: Oslo Metropolitan University, Pilestredet 35, 0130 Oslo, Norway.
  E-mail address: simkon@oslomet.no (S.S. Kongshaug).
  URL: https://oslomet.no (S.S. Kongshaug).

[1] An imposed strain field is strain incompatible if it does not satisfy the Saint-Venant's compatibility conditions.

expansion refers both to the strain incompatibility, e.g. the internal restraint from reinforcement, the non-linear ASR expansion fields over the height and width of a bridge, and the external restraint from boundary conditions, all leading to additional stresses in the structure.

For the structural engineer, put to task to conduct a structural assessment of an ASR-affected RC structure, two natural questions arise: (1) how to calculate the ASR-induced stresses, and (2), when the ASR-induced stresses are calculated, what is the residual capacity when accounting for the material deterioration caused by ASR?

The ASR-induced stresses may be calculated in a structural analysis that incorporates a concrete material model that includes ASR-induced concrete expansion. However, the correctness of the calculated stresses depends on the correctness of the imposed ASR strain field, which is (in general) unknown for an existing structure. Indeed, any structural application of any advanced material model that includes the effects of ASR will face the issue of identifying the imposed ASR expansion field, which may lead to substantial stresses, and which may substantially influence the prediction of the capacity. Although the model accounts for the effect of moisture and temperature on the ASR expansion, the problem is passed on to identify the moisture and temperature history (the variation in both space and time).

In the context of structural mechanics, any ASR related structural problem (solved using any concrete material model that incorporates the effects of ASR expansion) can be grouped into two kinds based on the knowledge of the input fields (predefined fields):

1. *The direct problem*, when the boundary and initial conditions for all the field variables (e.g. temperature and moisture) necessary to compute the ASR-induced expansion field are known a priori;
2. *The inverse problem*, when the history of the field variables is unknown, and must be deduced/reconstructed from field observations and measurements.

In well controlled experiments, the direct problem can be solved. In this case, the correctness of the solution, measured by the discrepancies between the solution of the structural problem and the experimental results, depends on the material model and the choice of material parameters. The best fit material parameters are the ones that reduce these discrepancies (which is another inverse problem). On the other hand, the structural analysis of an existing ASR-affected RC structure involves solving the inverse problem as the history of field variables is unknown. It is emphasized that the correctness of the solution of the inverse problem relies on a proper material model with known material parameters, i.e. it gives good predictions of the structural behaviour for the direct problem.

In this study, a state-of-the art concrete material model was used, which includes ASR expansion that relies on the input of a free ASR strain $\varepsilon^{\mathrm{asr,free}}$; it is interpreted as the ASR strain that would have occurred without stress (thus free).

The objective was to develop a suitable structural analysis approach to answer the first question stated above, i.e. finding the ASR-induced stresses. This method includes solving the inverse problem, where the task is to identify/reconstruct the time varying free ASR strain field $\varepsilon^{\mathrm{asr,free}}(\boldsymbol{x}, t)$, such that the structural analysis match some field measurements and observations. This is in general a mathematically ill-posed problem, as many such fields may lead to the same sets of measurements, but by limiting the solution space for $\varepsilon^{\mathrm{asr,free}}(\boldsymbol{x}, t)$, one can find a solution.

We developed an approach where the free ASR expansion field $\varepsilon^{\mathrm{asr,free}}(\boldsymbol{x}, t)$ is expressed as a linear combination of (predefined) functions, that in number is less than or equal to the number of displacement measurements. Many such fields can be stated and solved. Then, the calculated cracks can be used to assess the correctness of the assumed expansion field.

The material model and the structural analysis method were applied in a finite element analysis of a continuous beam bridge in Norway, Elgeseter bridge. The elongation of the bridge was used as the main observable, as part of solving the inverse problem, and the calculated cracks were used as the secondary observables in the assessment of the correctness. The results from the analysis of Elgeseter bridge were studied to increase the understanding of ASR-induced stresses in ordinary RC beam bridges.

2. 3D material model of ASR-affected concrete

The material model we used is a 3D generalization of a 1D model, proposed in our earlier work [6]. Among the different categories of ASR modelling approaches [7], this model falls in the category of models that depart from imposing an ASR expansion (strain) in concrete. The model includes the effect of ASR expansion, ASR-induced stiffness and tensile strength reduction, cracking, creep and compressive damage. These different concrete material effects are included by a decomposition of total strain[2] of the concrete into

$$\varepsilon = \varepsilon^{\mathrm{asr}} + \varepsilon^{\sigma} + \varepsilon^{\mathrm{cr}} + \varepsilon^{\mathrm{creep}}; \tag{1}$$

$\varepsilon^{\mathrm{asr}}$	is the imposed ASR strain. It is a function of the free ASR strain $\varepsilon^{\mathrm{asr,free}}$ (field variable), and stress, see Section 2.1 for the description of the constitutive model;
ε^{σ}	is the elastic strain, and represents the short term mechanical deformation. It is immediately reversible when the material is unloaded, thus elastic. This strain will be given by an isotropic stiffness relation for an undamaged material, while a rotating orthotropic stiffness relation is used for an ASR-damaged material. The constitutive model is described in Section 2.2;
$\varepsilon^{\mathrm{cr}}$	is the smeared crack strain, with the physical interpretation as a weaker/softer material that develops between the sound material. When a crack closes, the crack strain vanishes and the stiffness is recovered. The constitutive model is described in Section 2.3;
$\varepsilon^{\mathrm{creep}}$	is the creep strain. This is the time dependent deformation due to stress; for a constant stress it increases with time. The constitutive model is described in Section 2.4.

Similar decomposition of concrete strain, including creep strain, can be found in the work by van Zijl et al. [8,9].

To model compressive damage, we used an isotropic damage formulation, which is based on the concept of an effective stress. In this way, the stress is related to the effective stress by

$$\boldsymbol{\sigma} = (1 - \omega_{\mathrm{c}})\boldsymbol{\sigma}^{\mathrm{eff}}, \tag{2}$$

where $\boldsymbol{\sigma}^{\mathrm{eff}}$ is the effective stress, and ω_{c} is a damage variable ranging from 0 for an undamaged state to 1 for a completely damaged state, further elaborated in Section 2.5. Some of the strains listed above are related to the stress $\boldsymbol{\sigma}$, while others are related to the effective stress $\boldsymbol{\sigma}^{\mathrm{eff}}$.

2.1. ASR expansion model

We used an expansion based model similar to a model proposed by Wen [10], which is based on the following assumptions:

---

[2] Column matrix/vector representations of stress and strain tensors are used (Voigt notation). Matrices and vectors are written in bold.
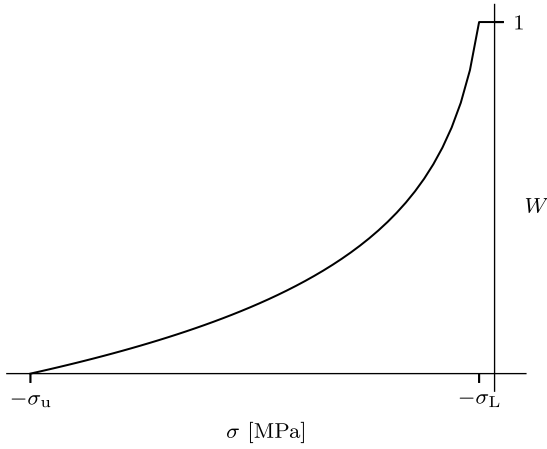
Fig. 1. $W(\sigma)$ expresses the imposed ASR expansion rate relative to the free ASR expansion rate (in any of the principal stress directions). The function proposed by Charlwood et al. [11] is assumed.

Fig. 2. Illustration of the series model for ASR-affected concrete: (a) concrete fibre of initial length L, (b) expands $\varepsilon^{\mathrm{asr}} L$ due to ASR, and (c) it strains ε^{σ} due to stress σ. A (3D) illustration of the series model is shown in (d).

1. The free ASR expansion $\varepsilon^{\mathrm{asr,free}}$—different from the imposed one—is a predefined field variable (input for the structural analysis). It is a scalar valued function of space and time, which is known for the direct problem and unknown for the inverse problem. It is a measure that represents the ASR strain that would occur without stress.

2. The imposed ASR expansion rate depends on the stress state, given by the instantaneous stress-expansion relationship

$$\dot{\varepsilon}^{\mathrm{asr}} = \mathbf{W}(\boldsymbol{\sigma}) \dot{\varepsilon}^{\mathrm{asr,free}}. \tag{3}$$

In Eq. (3), the over-dot denotes the time derivative, and $\mathbf{W}$ is a vector valued function of the stresses.

3. The imposed ASR expansion rate in any of the principal stress directions (with unit vectors $\bar{\mathbf{n}}_1$, $\bar{\mathbf{n}}_2$ and $\bar{\mathbf{n}}_3$) depends only on the principal stress in the same direction. It is also assumed that the ASR shear strain rates in the principal stress coordinates are zero. These assumptions leads to the following expression for the ASR expansion rate in the principal stress coordinates:

$$
\begin{aligned}
\dot{\bar{\varepsilon}}^{\mathrm{asr}} &= \bar{\mathbf{W}}(\bar{\boldsymbol{\sigma}}) \dot{\varepsilon}^{\mathrm{asr,free}} \\
&= \begin{bmatrix} W(\bar{\sigma}_1) \\ W(\bar{\sigma}_2) \\ W(\bar{\sigma}_3) \\ 0 \\ 0 \\ 0 \end{bmatrix} \dot{\varepsilon}^{\mathrm{asr,free}}
\end{aligned} \tag{4}
$$

4. The instantaneous stress-expansion relationship W is given by the logarithmic function proposed by Charlwood et al. [11] (illustrated in Fig. 1), given by

$$
W(\sigma) = \begin{cases} 1 & \text{if} \quad \sigma \geq -\sigma_{\mathrm{L}} \\ 1 - \dfrac{\log(\sigma/-\sigma_{\mathrm{L}})}{\log(\sigma_{\mathrm{u}}/\sigma_{\mathrm{L}})} & \text{if} \quad -\sigma_{\mathrm{u}} \leq \sigma < -\sigma_{\mathrm{L}} \\ 0 & \text{if} \quad \sigma < -\sigma_{\mathrm{u}} \end{cases} \tag{5}
$$

where the material constant σ_{u} is the compressive stress for which the ASR expansion rate vanish, and the material constant σ_{L} is the compressive stress for which the ASR expansion rate equals the free ASR expansion rate. These material constants are uncertain and depend, among other things, on the concrete mix, and must be determined from restrained expansion experiments.

The validity of the third assumption depends (among other) on the concrete mix as different anisotropic expansion behaviours have been reported in the literature. Four expansion behaviours can be
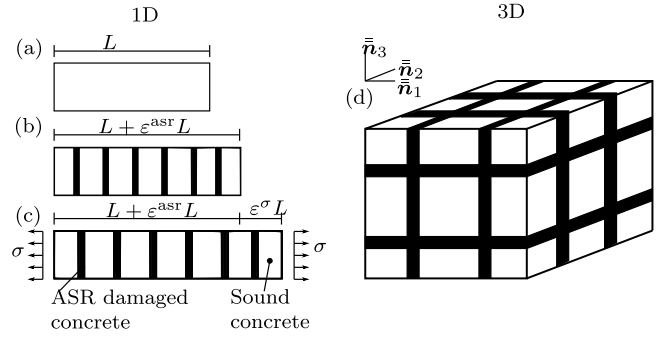
identified—if at least one direction is free of stress: (1) total transfer of expansion to the stress-free directions, i.e. volumetric expansion is preserved [2,12–14], (2) partial transfer of expansion [15–17], (3) no or negligible transfer to the stress-free directions [18,19], and (4) the expansion in the stress-free directions is reduced [20,21]. The expansion model, used in this study, is compliant with expansion behaviour (3).

The induced strain rate is transformed to the global coordinates by the relation:

$$\dot{\varepsilon}^{\mathrm{asr}} = \bar{\mathbf{T}}_{\sigma}^{\mathrm{T}} \dot{\bar{\varepsilon}}^{\mathrm{asr}}, \tag{6}$$

where $\bar{\mathbf{T}}_{\sigma}$ is the stress transformation matrix from global coordinates to principal stress coordinates, given by the relation $\bar{\boldsymbol{\sigma}} = \bar{\mathbf{T}}_{\sigma} \boldsymbol{\sigma}$.

2.2. Elastic compliance relation accounting for ASR stiffness damage

In this study, the elastic strain ε^{σ} represents the instant deformation due to stress, and it is given by the following compliance relation (expressed in global coordinates):

$$\boldsymbol{\varepsilon}^{\sigma} = \mathbf{C}^{\sigma} \boldsymbol{\sigma}^{\mathrm{eff}}. \tag{7}$$

To account for the increase in compliance (or reduction in stiffness) due to ASR, a series model inspired by the work of Wen [10] is developed, where the ASR-affected concrete is considered as being composed of sound concrete and ASR damaged concrete in series, see Fig. 2 for an illustration. The figure shows (1D) a material fibre with initial length L (Fig. 2a), which elongates $L_{\mathrm{asr}} = \varepsilon^{\mathrm{asr}} L$ due ASR (Fig. 2b). The sound concrete has a stiffness equal to the modulus of elasticity E_0, and the damaged concrete has a reduced modulus of elasticity $E_{\mathrm{asr}} = \beta_{\mathrm{E}}^{\mathrm{asr}} E_0$, where $\beta_{\mathrm{E}}^{\mathrm{asr}}$ is a coefficient. The elongation $\varepsilon^{\sigma} L$ due to stress (Fig. 2c) is composed of two parts: the elongation of the sound material, and that of the ASR damaged material, both assumed linearly related to stress, see Eq. (8).

$$
\begin{aligned}
\varepsilon^{\sigma} L &= \varepsilon^{\sigma,\mathrm{sound}} L + \varepsilon^{\sigma,\mathrm{asr}} L_{\mathrm{asr}} \\
&= \frac{\sigma^{\mathrm{eff}}}{E_0} L + \frac{\sigma^{\mathrm{eff}}}{\beta_{\mathrm{E}}^{\mathrm{asr}} E_0} \varepsilon^{\mathrm{asr}} L \\
\varepsilon^{\sigma} &= \left(\frac{1}{E_0} + \frac{\varepsilon^{\mathrm{asr}}}{\beta_{\mathrm{E}}^{\mathrm{asr}} E_0} \right) \sigma^{\mathrm{eff}}
\end{aligned} \tag{8}
$$

The above expression for ASR-induced increase in compliance (or equivalently reduction in stiffness), is also used in the works of [22–25], where the value of $\beta_{\mathrm{E}}^{\mathrm{asr}} = 0.003$ was used. In the experimental investigation by Kongshaug et al. [26], $\beta_{\mathrm{E}}^{\mathrm{asr}} = 0.0033$ gave the best fit.

In this work, the 1D series model is generalized to 3D, see Fig. 2d for an illustration. The model can be characterized as a rotating orthotropic elastic damage law, with material directions aligned with the principal ASR strain directions with unit vectors $\bar{\mathbf{n}}_i$. In the coordinates aligned

with the principal ASR strain directions, the compliance relation reads

$$\bar{\bar{C}}^{\sigma} = C^{\text{el}} + \bar{\bar{C}}^{\sigma,\text{asr}}, \tag{9}$$

where C^{el} is the isotropic elastic compliance matrix, defined by the two independent material constants modulus of elasticity E_0 and Poisson's ratio ν, and $\bar{\bar{C}}^{\sigma,\text{asr}}$ is an orthotropic compliance matrix, given by

$$\bar{\bar{C}}^{\sigma,\text{asr}} =$$

$$\begin{bmatrix} \frac{\bar{\varepsilon}_1^{\text{asr}}}{\beta_{\text{E}}^{\text{asr}} E_0} & 0 & 0 & 0 & 0 & 0 \\ 0 & \frac{\bar{\varepsilon}_2^{\text{asr}}}{\beta_{\text{E}}^{\text{asr}} E_0} & 0 & 0 & 0 & 0 \\ 0 & 0 & \frac{\bar{\varepsilon}_3^{\text{asr}}}{\beta_{\text{E}}^{\text{asr}} E_0} & 0 & 0 & 0 \\ 0 & 0 & 0 & \frac{\bar{\varepsilon}_1^{\text{asr}}+\bar{\varepsilon}_2^{\text{asr}}}{\beta_{\text{G}}^{\text{asr}} G_0} & 0 & 0 \\ 0 & 0 & 0 & 0 & \frac{\bar{\varepsilon}_1^{\text{asr}}+\bar{\varepsilon}_3^{\text{asr}}}{\beta_{\text{G}}^{\text{asr}} G_0} & 0 \\ 0 & 0 & 0 & 0 & 0 & \frac{\bar{\varepsilon}_2^{\text{asr}}+\bar{\varepsilon}_3^{\text{asr}}}{\beta_{\text{G}}^{\text{asr}} G_0} \end{bmatrix}, \tag{10}$$

where $\bar{\varepsilon}_i^{\text{asr}}$ (for $i = 1, 2, 3$) are the principal ASR strains. The coefficient $\beta_{\text{G}}^{\text{asr}}$ determines the rate of increase in shear compliance. Due to lack of mechanical testing on determining its value, we assume that the two coefficients are equal $\beta_{\text{G}}^{\text{asr}} = \beta_{\text{E}}^{\text{asr}}$.

The expression for the compliance relation, expressed in global coordinates (Eq. (7)) is now written

$$\begin{aligned} \boldsymbol{\varepsilon}^{\sigma} &= \bar{\bar{T}}_{\sigma}^{\text{T}} \bar{\bar{\varepsilon}}^{\sigma} \\ &= \bar{\bar{T}}_{\sigma}^{\text{T}} \bar{\bar{C}}^{\sigma} \bar{\bar{T}}_{\sigma} \boldsymbol{\sigma}^{\text{eff}} \\ &= \underbrace{\left[C^{\text{el}} + \bar{\bar{T}}_{\sigma}^{\text{T}} \bar{\bar{C}}^{\sigma,\text{asr}} \bar{\bar{T}}_{\sigma} \right]}_{C^{\sigma} \text{ in } (7)} \boldsymbol{\sigma}^{\text{eff}} \end{aligned} \tag{11}$$

where $\bar{\bar{T}}_{\sigma}$ is the stress transformation matrix from global to principal ASR strain coordinates.

2.3. Fixed orthotropic smeared crack model for stress induced macro crack

A sufficient tensile stretching of concrete leads to strain localization over a characteristic length, denoted crack band, which finally results in development of a macro crack. In the crack band and in the macro crack, softening occurs, i.e. decreasing stress with increasing strains, while the material on each side experiences elastic unloading. This can be modelled by a continuum approach with the concept of a smeared crack strain, and a softening material law.

Strain localization will also occur in a numerical solution by use of the displacement based finite element method (FEM) when the material is softening. Then, the strain localizes in a *numerical* crack band, which in length typically equals the length of the finite element (if linear interpolation is used). Consequently, the solution depends on the mesh refinement. To make the solution objective with respect to mesh refinement, the crack band method [27] is applied. In this approach, the material model (in tension) depends on the size and order of the finite element such that the dissipated energy (fracture energy) is less mesh size dependent.

The material model should also depend on the expected number of cracks within each finite element. This is important when modelling RC structures where several cracks might be expected depending on the crack spacing. For numerical solutions with the displacement based finite element method, the numerical crack band width should be chosen based on the size and order of the finite element, and the crack spacing. Discussion on upper and lower bounds of the numerical crack band width (localization limiters) are discussed in [28]. In more advanced crack band models, the material model also depends on the orientation of cracks wrt mesh [29,30], and [31]. This refinement is not adopted here.

The relation between crack strain and effective stress in the fixed local orthogonal crack coordinate system is given by the compliance relation

$$\bar{\bar{\varepsilon}}^{\text{cr}} = \bar{\bar{C}}^{\text{cr}} \bar{\bar{\sigma}}^{\text{eff}}, \tag{12}$$

where compliance matrix is assumed as follows:

$$\bar{\bar{C}}^{\text{cr}} = \begin{bmatrix} \bar{\bar{C}}_{11}^{\text{cr}} & 0 & 0 & 0 & 0 & 0 \\ 0 & \bar{\bar{C}}_{22}^{\text{cr}} & 0 & 0 & 0 & 0 \\ 0 & 0 & \bar{\bar{C}}_{33}^{\text{cr}} & 0 & 0 & 0 \\ 0 & 0 & 0 & \bar{\bar{C}}_{44}^{\text{cr}} & 0 & 0 \\ 0 & 0 & 0 & 0 & \bar{\bar{C}}_{55}^{\text{cr}} & 0 \\ 0 & 0 & 0 & 0 & 0 & \bar{\bar{C}}_{66}^{\text{cr}} \end{bmatrix}, \tag{13}$$

with

$$\bar{\bar{C}}_{ii}^{\text{cr}} = \frac{\alpha_i^{\text{cr}} H(\bar{\bar{\sigma}}_i)}{\sigma_i^{\text{cr}}(\alpha_i^{\text{cr}})} \text{ for } i = 1, 2, 3$$

$$\bar{\bar{C}}_{44}^{\text{cr}} = \max\{\bar{\bar{C}}_{11}^{\text{cr}}, \bar{\bar{C}}_{22}^{\text{cr}}\}/r_g$$

$$\bar{\bar{C}}_{55}^{\text{cr}} = \max\{\bar{\bar{C}}_{11}^{\text{cr}}, \bar{\bar{C}}_{33}^{\text{cr}}\}/r_g$$

$$\bar{\bar{C}}_{66}^{\text{cr}} = \max\{\bar{\bar{C}}_{22}^{\text{cr}}, \bar{\bar{C}}_{33}^{\text{cr}}\}/r_g.$$

α_i^{cr} is the maximum crack strain obtained for crack i with crack normal $\bar{\bar{n}}_i$, and $\sigma_i^{\text{cr}}(\alpha_i^{\text{cr}})$ is the corresponding crack strength. r_g is similar to the crack shear stiffness coefficient in Ref. [32], which recommends a value between 1 and 10. $\bar{\bar{n}}_1$ is the normal of the first crack, and is determined as the maximum principal stress direction at the onset of cracking. $\bar{\bar{n}}_2$ is determined by violation of the crack criterion in a direction orthogonal to $\bar{\bar{n}}_1$, and $\bar{\bar{n}}_3$ is determined from $\bar{\bar{n}}_1$ and $\bar{\bar{n}}_2$ (by the condition of orthogonality). The heavy side function H is used to restore the initial stiffness (or zero crack compliance) for closed cracks.

The maximum crack opening of crack i w_i^{cr} is equal the maximum crack strain α_i^{cr} multiplied with the numerical crack bandwidth h (size of the finite element):

$$w_i^{\text{cr}} = \alpha_i^{\text{cr}} h; \quad \alpha_i^{\text{cr}} = \max(\bar{\bar{\varepsilon}}_i^{\text{cr}}). \tag{14}$$

In this way, the tensile strength of the concrete σ_i^{cr} (for crack i) can be expressed as a decreasing/softening function of the maximum crack opening, e.g., the function proposed by [33].

For large scale unreinforced structures, analysed using large elements, a solution to avoid snap-back is to use the brittle crack model, Eq. (15), but it is emphasized that this approach is not objective with mesh refinement as the dissipated energy is proportional with the characteristic size of the cracked elements.

$$f_{\text{br}} = \begin{cases} f_{\text{ct0}} & \text{if} \quad \alpha^{\text{cr}} = 0 \\ 0.01 f_{\text{ct0}} & \text{if} \quad \alpha^{\text{cr}} > 0 \end{cases} \tag{15}$$

For large scale reinforced concrete structures, analysed using large elements, the post peak behaviour is usually not dominated by a single crack within each element, but rather distributed cracking due to the bond action between concrete and reinforcement, termed the tension-stiffening effect. This effect can be included by modification of the softening behaviour of the concrete in the neighbourhood of the reinforcement [34], but this is, however, not adopted in this study.

The micro cracking due to ASR reduces the tensile strength of the material. This was modelled by an isotropic damage law given by the same damage law as for the stiffness reduction. The softening law now reads:

$$\sigma_i^{\text{cr}} = \left(1 - \frac{\varepsilon_{\text{max}}^{\text{asr}}}{\varepsilon_{\text{max}}^{\text{asr}} + \beta_{\text{f}_{\text{ct}}}^{\text{asr}}} \right) f_{\text{br}}, \tag{16}$$

where $\varepsilon_{\text{max}}^{\text{asr}} = \max\{\bar{\bar{\varepsilon}}_i^{\text{asr}}\big|_{t_{\text{cr}}} : i = 1, 2, 3\}$, where t_{cr} is the time at cracking, and $\beta_{\text{f}_{\text{ct}}}^{\text{asr}}$ is a coefficient fitted to the experimental results of Smaoui et al. [35], see Fig. 3. They measured the direct tensile strength
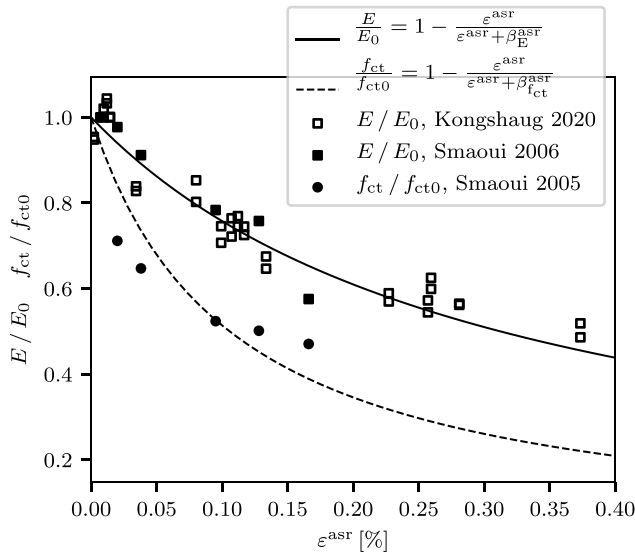
Fig. 3. The evolution of relative modulus of elasticity in Refs. [26,35] are similar; the curve fit (least square method) is only applied to the data from Ref. [35], which gives $\beta_E^{asr} = 0.003$. The curve fit on the relative tensile strength adapted from Ref. [35] gives $\beta_{f_{ct}}^{asr} = 0.001$.

and modulus of elasticity for an ASR-affected concrete with similar evolution for modulus of elasticity as in [26].

Cracking ($\dot\alpha_i^{cr} \geq 0$) is controlled by a Rankine fracture criterion for each crack $i = 1, 2, 3$, given by

$$F_i^{cr} = \bar{\bar{\sigma}}_i^{eff} - \sigma_i^{cr}(w_i^{cr}(\alpha_i^{cr})) \leq 0, \tag{17}$$

with the conditions

$$\dot\alpha_i^{cr} \geq 0, \quad F_i^{cr}\,\dot\alpha_i^{cr} = 0. \tag{18}$$

The crack compliance relation in global coordinates is

$$\boldsymbol{\varepsilon}^{cr} = \bar{\bar{\boldsymbol{T}}}_\sigma^T\,\bar{\bar{\boldsymbol{C}}}^{cr}\,\bar{\bar{\boldsymbol{T}}}_\sigma\,\boldsymbol{\sigma}^{eff} \tag{19}$$

where $\bar{\bar{\boldsymbol{T}}}_\sigma$ is the stress transformation matrix from global to the fixed crack coordinate system.

2.4. Creep model

Concrete creep is modelled using ageing isotropic linear viscoelasticity, for which the creep strain at time[3] t is given by

$$\boldsymbol{\varepsilon}^{creep}(t) = \hat{\boldsymbol{C}}\int_{\tau=0}^{t} C^{creep}(t, \tau)\dot\sigma\,d\tau, \tag{20}$$

where $\hat{\boldsymbol{C}}$ is a dimensionless matrix, given in Eq. (21), which establishes the three dimensional effect of creep, and $C^{creep}(t, \tau)$ is a creep function which gives the creep strain at time t for a unit stress applied at time τ.

$$\hat{\boldsymbol{C}} = E_0\boldsymbol{C}^{el} =$$

$$\begin{bmatrix} 1 & -\nu & -\nu & 0 & 0 & 0 \\ -\nu & 1 & -\nu & 0 & 0 & 0 \\ -\nu & -\nu & 1 & 0 & 0 & 0 \\ 0 & 0 & 0 & 2(1+\nu) & 0 & 0 \\ 0 & 0 & 0 & 0 & 2(1+\nu) & 0 \\ 0 & 0 & 0 & 0 & 0 & 2(1+\nu) \end{bmatrix} \tag{21}$$

We used the creep function given in Eurocode [36], $C^{creep}(t, \tau) = \frac{\phi}{E_0}$, where the function ϕ denotes the creep coefficient. To achieve a numerically efficient solution procedure, a five-unit Kelvin chain is first fitted to the Eurocode creep function. The procedure of function fitting is described in Ref. [6].

2.5. Isotropic damage model for compressive crushing

Concrete in compression experience strain localization due to softening instability, which result in a size effect as for tension. As explained for tensile cracking, numerical simulation with the FEM with a compressive softening material requires a suitable regularization technique to obtain mesh objective energy dissipation. The approach by [37], denoted "crush band method" is used. This is an extension of the crack band theory [27] to compressive behaviour; it is assumed that compressive fracture energy G_c is a material property, and that strains localize into a numerical crush band, h_c. Damage due to compression is modelled with a Drucker Prager isotropic damage law. The scalar damage variable ω_c relates the stress to the effective stress, see Eq. (2). It is a function of a monotonic increasing scalar state variable $\varepsilon_{c,max}$, which is the maximum obtained value of a strain-like measure ε_c;

$$\varepsilon_{c,max} = \max(\varepsilon_c) \tag{22}$$

$$\varepsilon_c = \frac{0.2}{E_0}I_1^{\sigma^{eff}} + \frac{1.2}{E_0}\sqrt{3J_2^{\sigma^{eff}}} \tag{23}$$

The strain-like measure ε_c equals, in absolute sense, the elastic strain of the sound material, for uniaxial compression loading, i.e. if the material is loaded in $\bar{n}_1$-direction, then $\varepsilon_c = \left|\bar\varepsilon_1^{\sigma,sound}\right|$. In Eq. (23), $I_1^{\sigma^{eff}}$ is the first invariant of the effective stress, and $J_2^{\sigma^{eff}}$ is the second invariant of the deviatoric effective stress. These are expressed in terms of the principal effective stresses in Eq. (24).

$$\begin{aligned} I_1^{\sigma^{eff}} &= \bar\sigma_1^{eff} + \bar\sigma_2^{eff} + \bar\sigma_3^{eff} \\ J_2^{\sigma^{eff}} &= \frac{1}{6}\left[(\bar\sigma_1^{eff} - \bar\sigma_2^{eff})^2 + (\bar\sigma_2^{eff} - \bar\sigma_3^{eff})^2 + (\bar\sigma_3^{eff} - \bar\sigma_1^{eff})^2\right] \end{aligned} \tag{24}$$

It is assumed that damage starts evolving at a threshold ε_{c0}, so $\omega_c = 0$ when $\varepsilon_{c,max} \leq \varepsilon_{c0}$. After damage initiation, the stress strain relation in uniaxial compression is assumed to have a parabolic form, see Fig. 4, which leads to the expression in Eq. (25) for the scalar compressive damage variable (see Eq. (25) in Box I).

It should be noticed that the above damage law is also defined for tension loading (because ε_c is not vanishing for tension), but will, however, not be activated for tension dominated loading. This is because the three Rankine criteria will be activated first, and hence limit the effective stress. In Fig. 5, the initial and peak compressive damage surfaces (converted to stress space) have been plotted for biaxial radial loading.[4] Only the part of the isotropic damage surface that might be violated is shown, in addition to the Rankine criteria/surface.

The influence of ASR on the compressive strength is neglected in this model. Experimental studies show divergent and only minor effects of ASR on the compressive strength, in particular for expansion levels observed in real structures.

3. Method for identifying the ASR-induced stresses: the inverse structural ASR problem, the solution procedure and the structural crack evaluation

A method was developed to identify the ASR-induced stresses, which involves (1) stating one or multiple inverse problem(s), (2) solution procedure for the inverse problem(s), and (3) an evaluation of calculated crack pattern.

---

[3] We assume that the structure is stress free up to concrete age of 28 days, and therefore, the choose the time variables t and τ to measure the time, in days [d], from 28 days after casting.

[4] Radial loading means that the stress σ is increased/decreased by a scalar λ, given by $\sigma = \lambda\,\sigma_{initial}$, where $\sigma_{initial}$ is a constant vector.

$$\omega_c = \begin{cases} 0 & \text{if} \quad \varepsilon_{c,max} < \varepsilon_{c0} \\ 1 - \dfrac{\varepsilon_{c0}}{\varepsilon_{c,max}}\left(1 + 4\dfrac{\varepsilon_{c,max}-\varepsilon_{c0}}{\varepsilon_{cp}-\varepsilon_{c0}} - 2\left(\dfrac{\varepsilon_{c,max}-\varepsilon_{c0}}{\varepsilon_{cp}-\varepsilon_{c0}}\right)^2\right) & \text{if} \quad \varepsilon_{c0} < \varepsilon_{c,max} \leq \varepsilon_{cp} \\ 1 - 3\dfrac{\varepsilon_{c0}}{\varepsilon_{c,max}}\left(1 - \left(\dfrac{\varepsilon_{c,max}-\varepsilon_{cp}}{\varepsilon_{cu}-\varepsilon_{cp}}\right)^2\right) & \text{if} \quad \varepsilon_{cp} < \varepsilon_{c,max} \leq \varepsilon_{cu} \\ 1 & \text{if} \quad \varepsilon_{cu} < \varepsilon_{c,max} \end{cases} \tag{25}$$

$$\varepsilon_{c0} = \frac{f_c}{3E_0}; \quad \varepsilon_{cp} = 5\,\varepsilon_{c0}; \quad \varepsilon_{cu} = \varepsilon_{cp} + \frac{3G_c}{2\,h_c\,f_c}$$
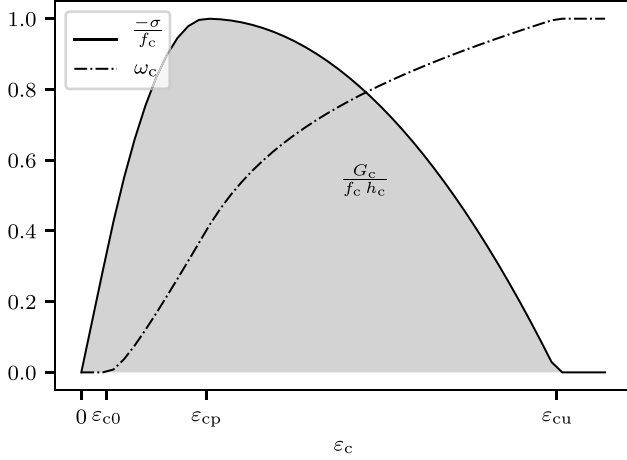
Box I.

Fig. 4. Stress–strain relationship for uniaxial compression loading, and the evolution of the scalar damage variable.
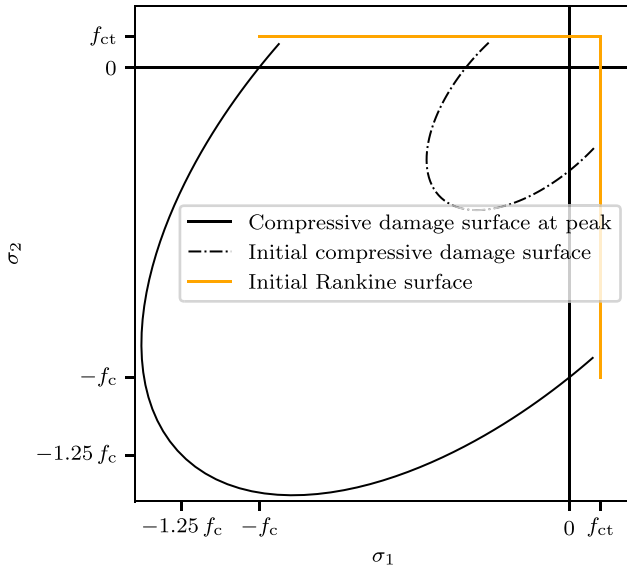

Fig. 5. The evolution of damage surface in principal stress space for biaxial radial loading. It evolves from the initial to the peak damage surface, before contraction due to compressive softening.

The inverse problem. Field measured displacements are used as the main observations in the inverse problem. To construct a well-posed inverse problem of identifying the free ASR expansion field (from field observations), the solution space of $\varepsilon^{asr,free}$ is limited to a function with a finite number of unknown coefficients β_j, $j = 1, 2, \ldots, n$, in

which number n is less than or equal to the number m of measured displacements, i.e. $n \leq m$. The free ASR expansion field $\varepsilon^{asr,free}$ is assumed as a linear combination of functions $\psi_j(x_1, x_2, x_3)$ of the spatial coordinates x_i, given by

$$\varepsilon^{asr,free}(\boldsymbol{x}, t) = \frac{t}{t_{end}} \sum_{j=1}^n \beta_j \psi_j(x_1, x_2, x_3) = \frac{t}{t_{end}} \boldsymbol{\beta}^T \boldsymbol{\psi}. \tag{26}$$

It is noticed that the field is linear in time t, despite the s-shaped evolution of ASR expansion often observed for experiments in highly ASR-accelerated environments. The inverse problem is to determine the unknown vector of coefficients $\boldsymbol{\beta}$, such that some field measured displacements, collected in a vector $\boldsymbol{d}^{obs}$, are close to the corresponding calculated displacements $\boldsymbol{d}^s = \boldsymbol{a}^{obs} \boldsymbol{d}$ from the finite element analysis. Here, $\boldsymbol{a}^{obs}$ is a topology matrix (of ones and zeros), which extracts the corresponding displacements ($\boldsymbol{d}^s$) from the structural displacement vector evaluated at the end time (t_{end}) of the structural analysis $\boldsymbol{d} = \boldsymbol{d}|_{t_{end}}$. It is emphasized that the structural displacement vector $\boldsymbol{d}$ depends on the unknown parameters $\boldsymbol{\beta}$. To measure the closeness, we establish an objective function that measures the error between simulation and field measurements:

$$s = \sum_{i=1}^m r_i^2 = \sum_{i=1}^m (d_i^{obs} - d_i^s)^2 = \|\boldsymbol{d}^{obs} - \boldsymbol{a}^{obs}\boldsymbol{d}\|^2 \tag{27}$$

The objective is now to find the parameters that minimize the error s, which reads

$$\min_{\boldsymbol{\beta} \in \mathcal{B}} s; \quad \mathcal{B} \subset \mathbb{R}^n \quad \dim(\boldsymbol{d}^{obs}) = m \geq n = \dim(\boldsymbol{\beta}) \tag{28}$$

where the construction of the functions ψ_j, determine the reasonable bounds for the set $\mathcal{B}$.

Solution procedure. If the inverse problem involves only one or two observations (in $\boldsymbol{d}^{obs}$) and unknown coefficients (in $\boldsymbol{\beta}$), a brute-force search might be an option (either by automatic or manual update of the unknown coefficients). The brute-force search becomes very time consuming for additional unknowns as it involves many trials of $\boldsymbol{\beta}$, where for each trial, a time consuming non-linear finite element analysis is conducted. A more sophisticated solution procedure is needed when several observations and unknown coefficients are involved. In Appendix, a Gauss–Newton algorithm to solve the inverse problem (Eq. (28)) is presented, where an analytical expression for the Jacobian $\boldsymbol{J} = -\frac{\partial \boldsymbol{r}}{\partial \boldsymbol{\beta}}$ is derived.

Structural crack evaluation/assessment. The cracks are seen as secondary observations, which are not used in solving the inverse problem, but which are used for verifying the correctness of the assumed free ASR expansion field. Or rather, one can only falsify the correctness of the assumptions.

Multiple inverse problems, i.e. alternative free ASR expansion fields, can be stated and solved. Then, the calculated cracks can be compared with the field observations to come closer to the real ASR-induced expansion field, and thus, the ASR-induced stresses. The choice of the solution space for the causal variable ε^{asr}, i.e. the choice of functions
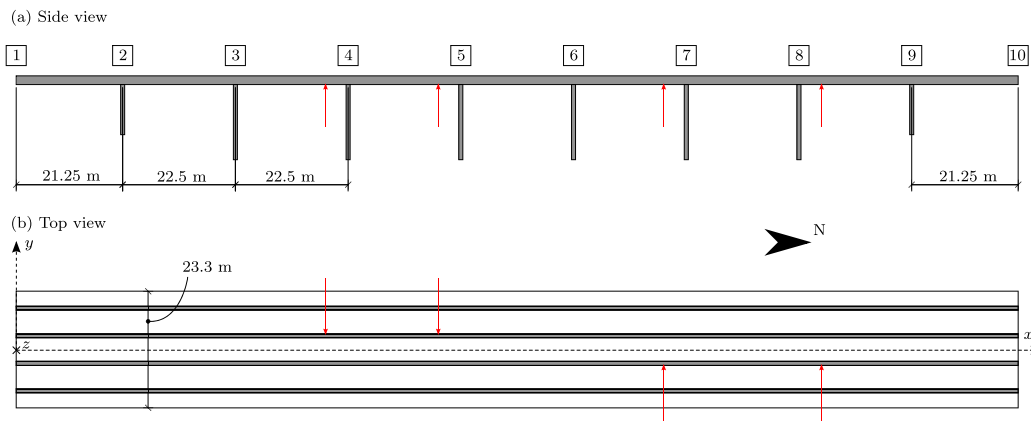
(a) Side view

(b) Top view

Fig. 6. Drawing of Elegeseter bridge. The locations of large cracks (crack widths up to 6 mm) are marked with red arrows.
Source: Adapted from [38].

Fig. 7. There is a sign of water penetration of the bridge deck in outermost region of the bridge. The image shows the western outer and western inner beam. Image courtesy of Dr. Ing. A. Aas-Jakobsen AS.

ψ in Eq. (26), should not be arbitrary, but based on information of the structure. This can be signs or tests indicating a certain moisture distribution.

4. Application to a real case: Elgeseter Bridge in Norway

4.1. Elgeseter Bridge

Our study was inspired and motivated by a real case, Elgeseter Bridge in Norway, which is affected by ASR. It is a 200 m long ordinary RC beam bridge of nine spans. The bridge deck is carried by four longitudinal beams, which are supported by slender columns, see Fig. 6; everything is made of monolithically cast reinforced concrete. In the recent years, the structural effects of ASR expansion of the bridge superstructure have become the primary concern [39,40]. ASR has resulted in an elongation of the bridge, which has been quantified through measurements of the width of the only expansion joint in the north end of the bridge, designed to be 200 mm wide. In 2003, the

width was reduced to near zero, which made repair of the expansion joint necessary. Based on the expansion joint measurements from 1962 to 2001, reported in [39], the current elongation of the bridge is estimated at 200 mm, which gives an average expansion of 0.1 %. In an inspection of the bridge in 2012 [38], it was observed that water penetrated though the bridge deck, likely due to punctuation of the water sealing, in the outermost part of the bridge on both sides, and throughout the bridge length, see Fig. 7. It has been believed, that this has resulted in a spatial moisture variation over both the height and the width, and therefore, variations in ASR expansion [39]. A variation in water content along the width of the bridge deck is documented [41].

In the same bridge inspection [38], large vertical cracks (up to 6 mm) in the inner beams were observed, see Fig. 8 for close-ups. The locations of these large cracks are shown in Fig. 6. In the span between axes 3 and 4 and in the span between axes 4 and 5, the large cracks are located only in the <u>western</u> inner beam. In the span between axes 6 and 7 and in the span between axes 8 and 9, the large cracks are located only in the <u>eastern</u> inner beam. All cracks have occurred 4.5 m

(a)

(b)

Fig. 8. Vertical crack in a region with low amount of reinforcement in an inner beam (a), which is measured in (b). Image courtesy of Dr. Ing. A. Aas-Jakobsen AS.

from the columns, where the amount of reinforcement is low, see Fig. 9. Based on the drawings, these cross sections consist of only three $\phi 32$ bars as longitudinal reinforcement. Nevertheless, if the reinforcement work was conducted with minor extensions and/or movements (in total <150 mm) of some reinforcing bars in these areas (resulting in overlapping), the amount of reinforcement in these sections can be considerably greater, which might explain the arbitrarily positioning of the large cracks. In the Norwegian Public Roads Administration (NPRA)'s digital database for bridges ("Brutus"), it is described that the inner beams in all spans have cracks widths up to 3 mm approximately 5 m from the columns, except the spans from axis 3 to 4 and 6 to 7 (which have the largest cracks up to 6 mm).

Table 1

The reinforcement intensity, area per unit width [mm²/mm], for sections P1 to P7 (bridge deck); t,x denotes the top layer in x direction, and b,y the bottom layer in y direction.

	P1	P2	P3	P4	P5	P6	P7
t,x	0	0.781	0.221	0.221	0.221	0.791	0.791
t,y	0	1.005	1.005	0.603	1.407	1.91	1.005
b,x	0.791	0.791	0.442	0.442	0.442	0	0
b,y	1.915	1.25	0.804	0.804	2	1.327	1.327

Table 2

The reinforcement intensity, area per unit width [mm²/mm], for sections B1 to B19 (bridge beams); t,x denotes the top layer in x direction, and b,y the bottom layer in y direction.

	B1	B2	B3	B4	B4W	B5	B6
t,x	34.18	34.18	34.18	34.18	34.18	5.026	5.026
t,y	1.809	1.809	1.809	1.809	1.809	1.809	1.809
b,x	15.08	9.05	7.04	6.032	3.016	6.032	10.56
b,y	0.402	0.402	0.402	0.402	0.402	0.402	0.402

	B7	B8	B9	B10	B11	B12	B13
t,x	5.026	5.026	5.026	5.026	38.2	38.2	38.2
t,y	1.809	1.809	1.809	1.809	1.809	1.809	1.809
b,x	13.57	15.58	18.6	20.61	6.032	13.07	15.08
b,y	0.402	0.402	0.402	0.402	0.402	0.402	0.402

	B14	B15	B16	B17	B18	B19
t,x	38.2	5.026	5.026	5.026	5.026	5.026
t,y	1.809	1.809	1.809	1.809	1.809	1.809
b,x	21.11	11.058	15.08	25.13	17.09	12.06
b,y	0.402	0.402	0.402	0.402	0.402	0.402

4.2. Finite element model

Elgeseter bridge was analysed using the finite element analysis software ABAQUS. Only the bridge superstructure (bridge deck and beams) was modelled, and it was discretized with 4-node shell elements (S4R). Based on the visual inspection [38] (described in Section 4.1), it was assumed that the free ASR expansion field is symmetric about the vertical centre plane of the bridge (the xz-plane along the bridge), and that it is constant along the bridge length. As a result of these assumptions, we modelled only the half of the cross section with symmetry displacement boundary conditions along the centre plane, see Figs. 10 and 11. The top surface was used as the reference surface for all shell elements. In this way, the correct offset of the beams wrt the bridge slab is accounted for in the model. The thicknesses of the shell elements was chosen to be 310 mm for the bridge deck, and 1740 mm for the beams. We chose five integration points in the bridge deck, and 11 points for the beams. Additional integration points were used for the reinforcement. The reinforcement was included with the "rebar layer"-feature (in the section definition for the shell). In this way the reinforcement is perfectly embedded (no slip) and the material model of the reinforcement is 1D in the specified direction of the rebar layer. The reinforcement layout was simplified to four layers: longitudinal (x) and transverse (y) in both the top and the bottom of each shell cross section. Both the top and bottom rebar layers were placed 59 mm from the top and bottom shell surface for both beam and deck. The reinforcement amount varies over the bridge, so the model was split into several regions which were assigned different reinforcement areas in the shell section definition. In the bridge deck, the reinforcement only varies in the transverse direction (y). The deck was divided into seven regions, which were assigned different sections labelled P1 to P7, see Fig. 11, where the reinforcement amounts are given in Table 1. In the beams, the reinforcement varies only in the longitudinal direction (x), see Fig. 12 and Table 2 for the modelled sections.

The concrete material model, described in Section 2, was implemented in ABAQUS with the user-defined material subroutine UMAT.
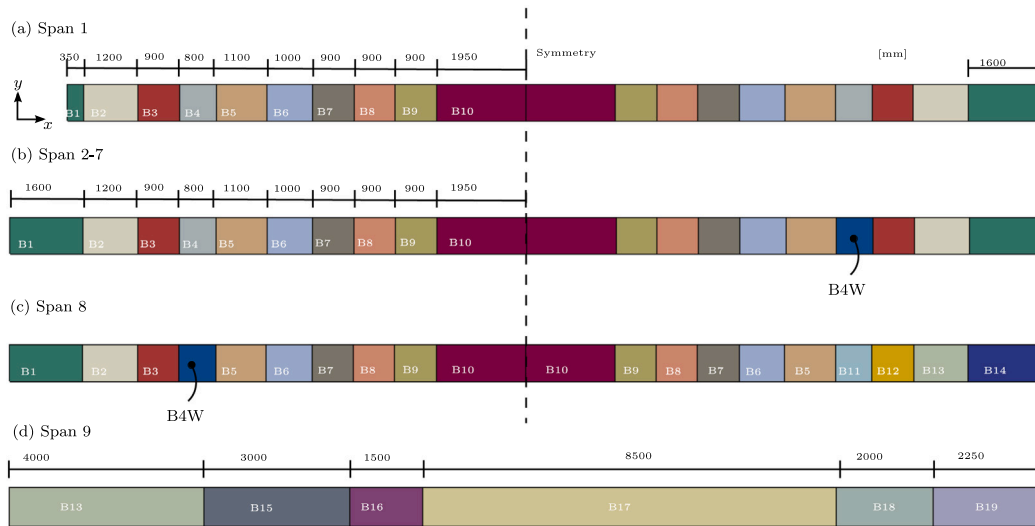
Fig. 9. Drawing of the reinforcement in the mid span beams of Elegeseter bridge [39]. The cross sections with low amount of reinforcement are marked in red. (For interpretation of the references to colour in this figure legend, the reader is referred to the web version of this article.)

Fig. 10. The dimension of the finite element model, and the displacement boundary conditions; the displacement in and rotation about the *x*-direction are denoted u_1 and ur_1, respectively (subindex 2 in *y*-direction and subindex 3 in *z*-direction).

Fig. 11. The dimensions of half the cross section of bridge. The different colours indicate different section definitions with different reinforcement amount. (For interpretation of the references to colour in this figure legend, the reader is referred to the web version of this article.)

Fig. 12. The beams are divided into regions and assigned different shell sections with different reinforcement amounts. In span 2-8, one week section, B4W, is included with only three $\phi 32$ bars in the bottom of the beam (approx 4.5 m from the columns, as observed on the bridge).
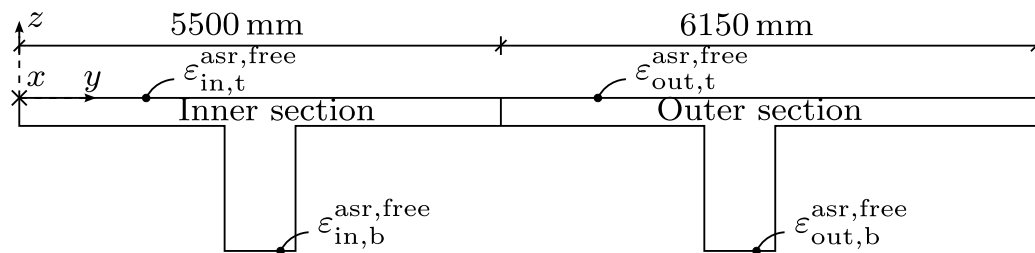
Fig. 13. The half bridge cross section was divided into an inner and an outer section, where each was assigned a vertically linearly varying free ASR expansion. The applied fields are expressed in terms of four (dependent) parameters, the bottom and top expansions in the inner and outer section: $\varepsilon_{\text{in,b}}^{\text{asr,free}}$, $\varepsilon_{\text{in,t}}^{\text{asr,free}}$, $\varepsilon_{\text{out,b}}^{\text{asr,free}}$ and $\varepsilon_{\text{out,t}}^{\text{asr,free}}$.

Table 3
Values for the material properties used in the structural analyses.

Material property	Symbol	Value
Concrete		
Concrete cylinder compressive strength	f_{c}	28 N/mm^2
Modulus of elasticity at an age of 28 days	E_0	23 313 N/mm^2
Concrete tensile strength	f_{ct0}	2.2 N/mm^2
ASR expansion parameter	σ_{u}	6 N/mm^2
ASR expansion parameter	σ_{L}	0.2 N/mm^2
ASR stiffness reduction parameter	$\beta_{\text{E}}^{\text{asr}}$	0.0033
ASR tensile strength reduction parameter	$\beta_{f_{\text{ct}}}^{\text{asr}}$	0.001
Steel		
Modulus of elasticity	E_{s}	200 000 N/mm^2
Initial yield stress	f_{sy}	340 N/mm^2
Hardening modulus	S	0.0001 · E_0 [N/mm^2]

Note: Material data are based on design information given on drawings. The concrete and the reinforcement steel are equivalent to class C25 (cube strength) and St 52, respectively, in the previous Norwegian code for design of concrete structures (NS 3473) [42], which still is used for assessment of existing structures.

We used the brittle crack model, as relatively large elements were used and the cracking occurred very locally. The reinforcement was modelled using the plasticity model in the ABAQUS material library. The value of the material properties that were used are summerized in Table 3.

Each FE analysis was divided into two analysis steps (load steps), where self-weight equal to 25 kN/m^3 was applied in the first step, and the free ASR expansion in the second step. The duration of each step and the number fixed time increments are summarized in Table 4.

Table 4
The duration (in days) and the number of fixed time increments of each analysis step (load step).

| Analysis step	Duration [days]	Increments
Step 1: Self-weight	1	20
Step 2: ASR expansion	25 185	100

4.3. The inverse problem, the solution procedure and the crack assessment of Elgeseter Bridge

Inverse problem. We assumed that we have only one main observable: the elongation of the bridge equal to (200 mm). In engineering practice, a global ASR expansion of a structure is often the most reliable and indisputable observation. The average displacement of the end nodes of the FE model was used to match the bridge elongation. As we have only one main observable, the assumed free ASR strain field can only include a single unknown β (in Eq. (26)) to make the inverse problem (Eq. (28)) well-posed. We investigated four alternative free ASR expansion fields (all expressed in only one unknown β), i.e. four independent inverse problems, which define four load combinations (LC), see Table 5 with further reference to Fig. 13. Similar variations in the free ASR expansion field were investigated in Refs. [6,39,40]. It is emphasized that the fields are hardly realistic, as the fields that influence ASR (moisture and temperature) are continuous.

Solution procedure. The inverse problem (Eq. (28)) was solved by calibrating the structural model, i.e. tuning the parameter β, to give the observed elongation of the bridge (brute-force search).
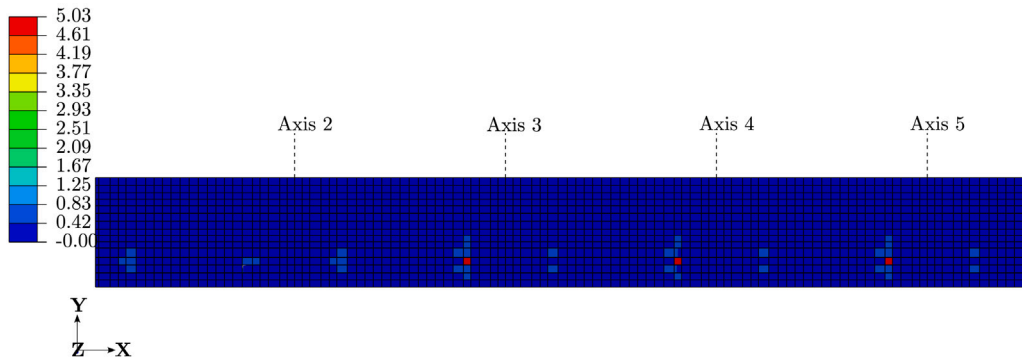
(a) First half (0-100 m) of the bridge.
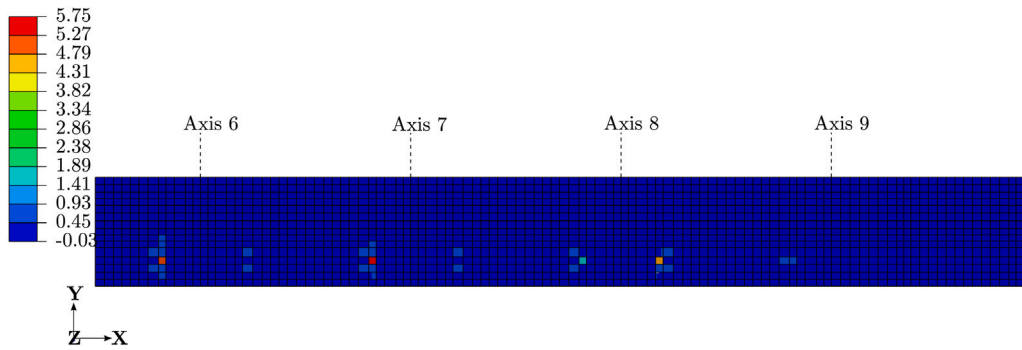
(b) Second half (100-200 m) of the bridge.

Fig. 14. ASR free expansion field LC 4. Crack width in mm (crack strain multiplied with FE length) in the *x*-direction on the <u>bottom</u> of the shells. The largest cracks occur in the beams.

Table 5
The four investigated free ASR expansion fields (LC 1-4).

	$\varepsilon_{in,b}^{asr,free}$	$\varepsilon_{in,t}^{asr,free}$	$\varepsilon_{out,b}^{asr,free}$	$\varepsilon_{out,t}^{asr,free}$
LC 1	β	β	β	β
LC 2	β	2β	2β	3β
LC 3	β	β	2β	2β
LC 4	β	β	4β	4β

Table 6
The solution of the four inverse problems, LC 1-4.

	$\varepsilon_{in,b}^{asr,free}$	$\varepsilon_{in,t}^{asr,free}$	$\varepsilon_{out,b}^{asr,free}$	$\varepsilon_{out,t}^{asr,free}$
LC 1	0.002	0.002	0.002	0.002
LC 2	0.00092	0.00184	0.00184	0.00276
LC 3	0.0014	0.0014	0.0028	0.0028
LC 4	0.00096	0.00096	0.00384	0.00384

Crack assessment. The calculated crack pattern for all of the load combinations was used for verifying the correctness of the different assumed ASR expansion fields. We could only falsify the correctness of these assumptions.

4.4. The solution of the inverse problems and the crack evaluation

The solutions of the four inverse problems, LC 1 to 4, are given in Table 6.

The ASR-induced structural cracks occurred mainly in the weak sections of the beams (B4W), approx. 4.5 m from the columns, see Fig. 14, which shows the crack widths (in mm) in the bottom of the shells for LC 4. No ASR-induced structural cracks occurred in the bridge deck, except in LC 4, where some cracks went through the thickness, see Fig. 15. The crack widths were calculated as the crack strain multiplied with the characteristic length of the elements. Fig. 16 summarizes the calculated crack widths through the height of the weak sections of inner beams for all LCs. From the inspection report of the bridge [38], the observed cracks in these sections extends from the bottom of the beams to the bridge deck, with a maximum crack opening of 6 mm. Based on the magnitude and the extension of the observed cracks, the free expansion fields in LC 1 and LC 3 were falsified, because the calculated crack widths are too small.

4.5. Comparison of the ASR-induced strains and stresses

For each LC, the calculated results in each span 1 to 7 were very much the same, while the results in span 8 and 9 differed from the rest. In the following, most of the results were taken from span 3 (between axes 3 and 4).

Because it is the imposed ASR expansion which causes the ASR-induced stresses, it was of interest to compare the calculated strains for the different load combinations. The imposed ε^{asr} and the free ASR expansion $\varepsilon^{asr,free}$ in the beams of span 3 are shown in Fig. 17 for the outer beam, and Fig. 18 for the inner beam. In Fig. 19, the same variables are plotted along transverse paths, *y*-direction, in (a) the mid span and (b) over the support/columns. We can observe the following:

- Even though there was a substantial difference between the free ASR expansion for LC 1–4, the imposed ASR expansion in the longitudinal direction (ε_x^{asr}) was similar for all LCs. Note that the imposed ASR in the shell normal direction ε_z^{asr} remained equal to the free ASR expansion due to the plane stress assumption.
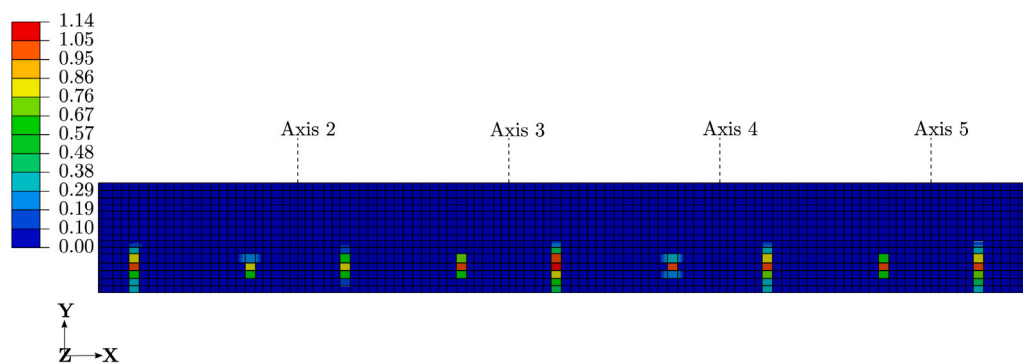
(a) First half (0-100 m) of the bridge (top view).
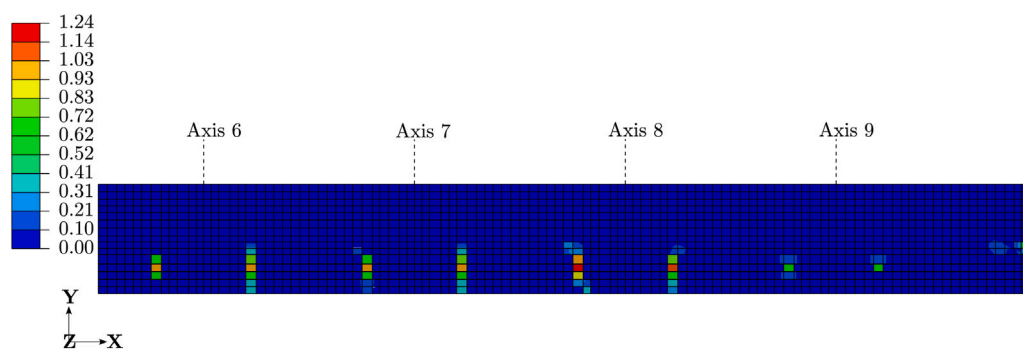
(b) Second half (100-200 m) of the bridge (top view).

Fig. 15. ASR free expansion field LC 4. Crack width in mm (crack strain multiplied with FE length) in the x-direction at the top of the shells.

- The great jumps in the free ASR expansion between the inner and outer sections vanished for the imposed expansion, see Fig. 19.
- The greatest difference in the imposed ASR expansion (ε_x^{asr}) between inner and outer beams were observed for LC 2 and LC 4. In these LCs, the imposed and the free ASR expansion were at some places almost coincident, which means that these regions experienced tension (or very small compressive stresses) during the history, i.e. W was close to 1 during the expansion process. Put differently, in these regions the imposed ASR expansion rate was limited by the free ASR expansion rate, and not the stress.
- The imposed expansion along the beams varied inversely to the reinforcement amount, see Fig. 20. This is clearly shown at the top of the beams in sub-figures (a) of Figs. 17 and 18, where a positive step in expansion coincides with a negative step in reinforcement amount.

The ASR-induced stress, $\Delta^{asr}\sigma$, was measured as the difference between the stress at the end of the two analysis steps—self-weight in step 1 and ASR expansion in step 2. Figs. 21 and 22 show the ASR-induced stress in the x-direction ($\Delta^{asr}\sigma_x$) in the concrete and reinforcement, respectively, for the beams in span 3 for LC 4. The pre-stressing effect is clearly observed with an increase in compressive stress in the concrete and tensile stress in the reinforcement. Moreover, the figures show that the ASR-induced stress in the concrete varied inversely to the stresses from self-weight alone. For instance, over the support, self-weight gave tensile stresses at the top and compressive stresses at the bottom of the beam sections, while the ASR-induced stress $\Delta^{asr}\sigma_x$ had the opposite sign. The ASR-induced reinforcement stresses (Fig. 22) were very large, especially where the reinforcement amount was small. At some locations the reinforcement yielded. The reinforcement yielded even at locations with no cracks, as in the weak sections of the outer beam in LC 4, see Fig. 23.

Even if the imposed ASR expansion became similar for all LCs, the differences were still sufficient to produce different crack widths as illustrated in Fig. 16. This holds in particular for the sections with low amount of reinforcement. This is supported by the calculated stresses in Fig. 21, which shows considerably larger tensile stresses in the inner than in the outer beam.

5. Discussion

Concrete material model and the method for identifying the ASR-induced stresses. The most sophisticated concrete material models that include the effects of ASR rely on many fields such as temperature, moisture and alkali content. In these advanced formulations (e.g. [25]) those fields are usually computed in time domain for the assumed boundary and initial conditions. Nevertheless, the boundary and initial conditions are (generally speaking) unknown for an existing structure, and consequently, limit the direct applicability of these models.

The concrete material model, presented in Section 2, and the method, presented in Section 3, give a suitable framework for assessing existing ASR-affected concrete structures. The ASR expansion model is based on only one scalar field variable, which is the free ASR expansion $\varepsilon^{asr,free}$, and therefore, only one unknown field. This simplifies the solution process. It should also be emphasized that the free ASR expansion is a sufficient starting point for modelling the material and structural effects of ASR. If one considers the more advanced models that depart from imposing an additional strain on the material level (e.g. [25] and Ref. [7] for an overview of such models), other fields as temperature, moisture and alkali content are, anyway, used to calculate the free ASR expansion as an intermediate step that is uncoupled from the mechanical problem.
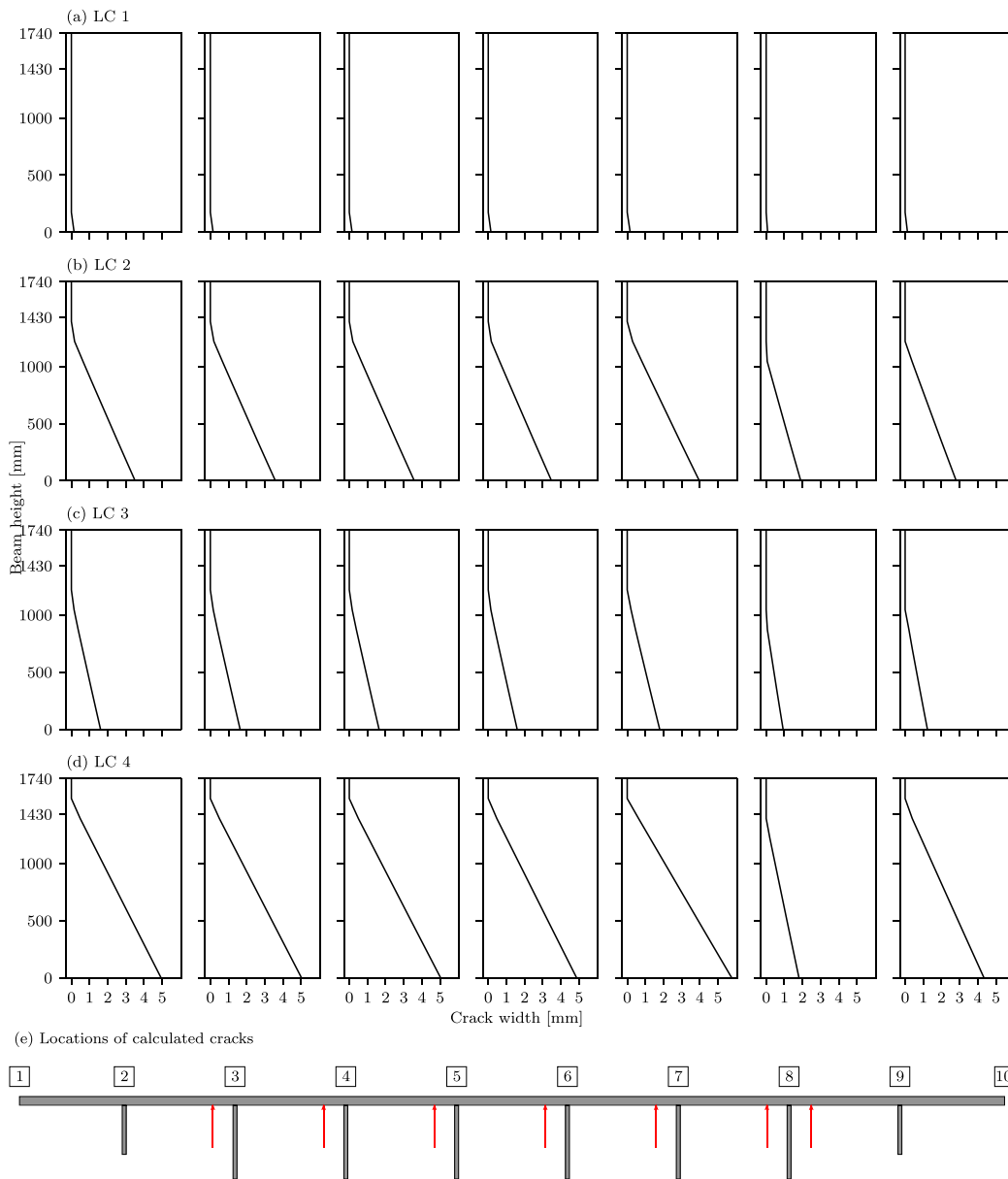
Fig. 16. Sub-figures (a)–(d) show the crack widths in LC 1–LC 4, in the weak sections (B4W) of the beams; the positions are marked with red arrows in (e).

It is emphasized that ASR expansion model (Section 2.1) in combination with the assumed linear evolution in time of the free ASR expansion (presented in Section 3) contradict experimental evidence showing a non-linear evolution in time. This means that we neglect (at least) two aspects which give rise to a non-linear expansion: (1) the influence of temperature on ASR rate, which in practice gives significant seasonal variations in expansion rate, and (2) the decrease of ASR rate due to exhaustion of the chemical reaction. The evolution of expansion (linear or non-linear) will influence the rate at which ASR-induced stresses are imposed, and consequently, the rate of creep. In general, creep has a stress-reducing effect on an imposed strain. In case of ASR, this might be counteracted by a greater imposed ASR expansion (due to the stress dependency). As a result, the final calculated stress, with or without the effect of creep, might similar. We believe that the importance of including creep increases when the sensitivity of the imposed ASR expansion to stress decreases.

The ASR expansion knowledge from the analysis of Elgeseter Bridge. Even though there is a substantial difference in *free* ASR expansion rate

between the outer and inner beam, the difference in imposed expansion rate in the longitudinal direction will after a certain time vanish because of the build-up of more compressive stress in the outer part than the inner part (said differently, after a certain time, both the inner and outer section will expand with the same rate).

The greater the sensitivity of the expansion to compressive stress (expressed by the shape of $W(\sigma)$ and the value σ_u), the more the imposed field changes/adapts from the shape of the free ASR expansion to a field giving lower stresses [6]. Since the sensitivity of compressive stress is so high, with W equal to the logarithmic function proposed by Charlwood et al. [11] and with $\sigma_u = 6$ MPa, the imposed ASR expansion in the longitudinal direction is similar for all of the four alternative free ASR expansion fields studied in Section 4. Consequently, the ASR-induced stresses are similar. The differences are still significant to cause different cracking behaviour. It is emphasized that this is not the case for the imposed ASR expansion in the direction normal to the bridge deck ε_z^{asr}, which equals to the free ASR expansion because of the plane stress assumption. Although the ASR-induced stresses are not very sensitive to the shape of the free ASR expansion field, the
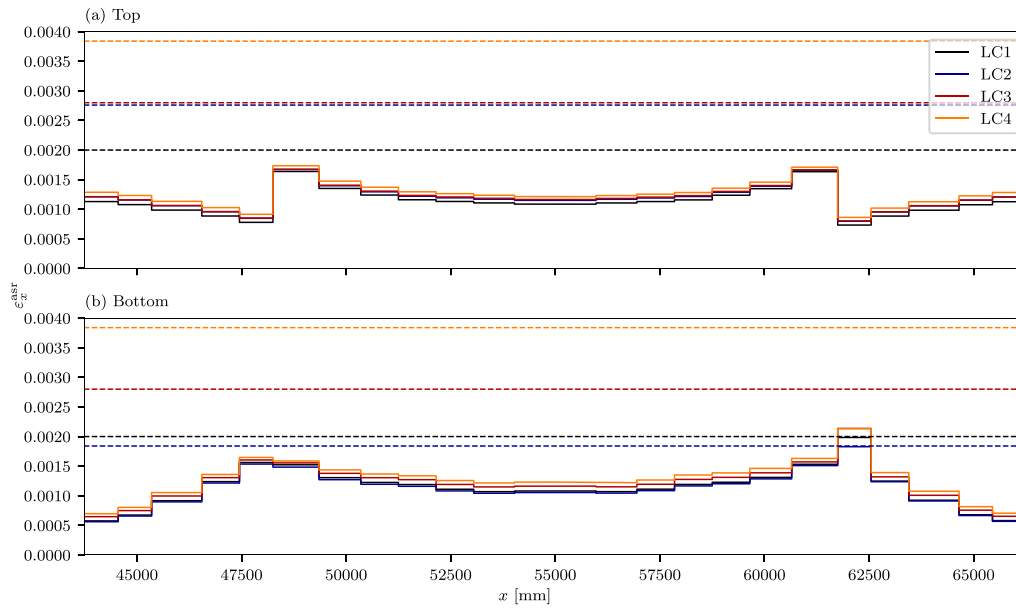
Fig. 17. Imposed ASR expansion in longitudinal direction x (ε_x^{asr}) in the <u>outer beam</u> of span 3 for all load combinations. Dashed lines are the corresponding free ASR expansion ($\varepsilon^{asr,free}$).
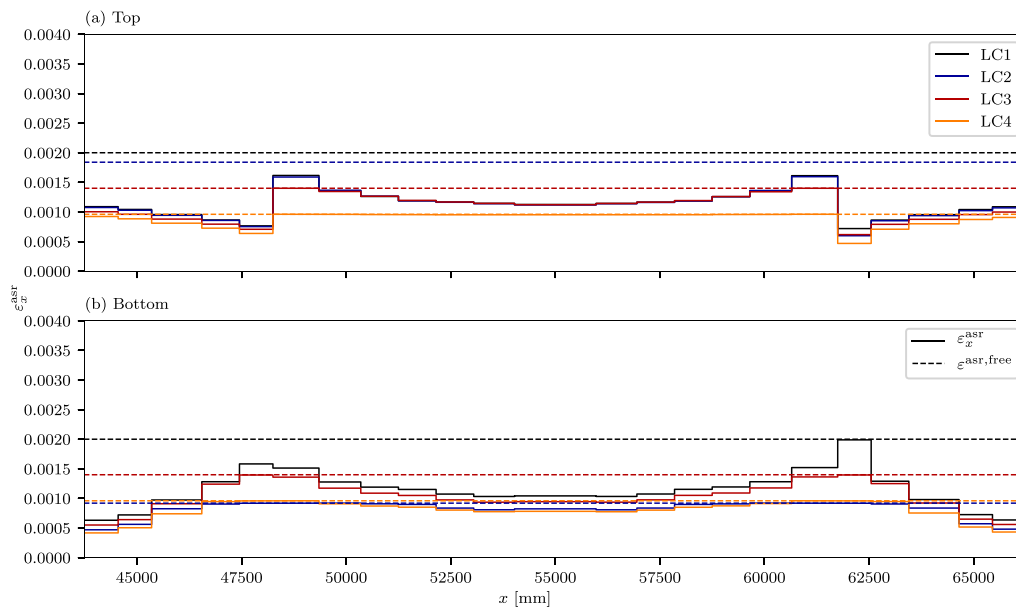

Fig. 18. Imposed ASR expansion in longitudinal direction x (ε_x^{asr}) in the <u>inner beam</u> of span 3 for all load combinations. Dashed lines are the corresponding free ASR expansion ($\varepsilon^{asr,free}$).

variation in material deterioration might be substantially different, and consequently, the variation in load bearing capacity might be of great importance.

The amount of reinforcement controls the variation of the imposed ASR expansion in the longitudinal direction of the bridge. The more reinforcement, the greater becomes the concrete compressive stress for a given expansion, and consequently, the imposed expansion is reduced.

In the proposed model, the absence of ASR expansion transfer between principal directions could explain the too large dependence of the expansion on stress. In particular, this might be of importance in case of 3D confinement, where the sensitivity to compressive stress might be substantially reduced, and Charlwood's law no longer is applicable. In this case, the obtained results are not conservative (reduced imposed stresses), because the reduction without lateral transfer or

other mechanism of gel absorption corresponds to a disappear of alkali gel.

6. Conclusions and further research

A concrete material model, which includes the effect of ASR expansion, ASR-induced stiffness and tensile strength reduction, cracking, creep and compressive damage, was developed (presented in Section 2). In this model, the ASR expansion relies on the input of only one predefined field variable—the free ASR expansion—interpreted as the expansion that would have occurred without stress. This field, and for the record any other ASR dependent field quantities, are in general unknown for an existing structure. So, a structural analysis method was developed, which is an approach to identify the unknown free ASR expansion, and thus the ASR-induced stresses (presented in Section 3).
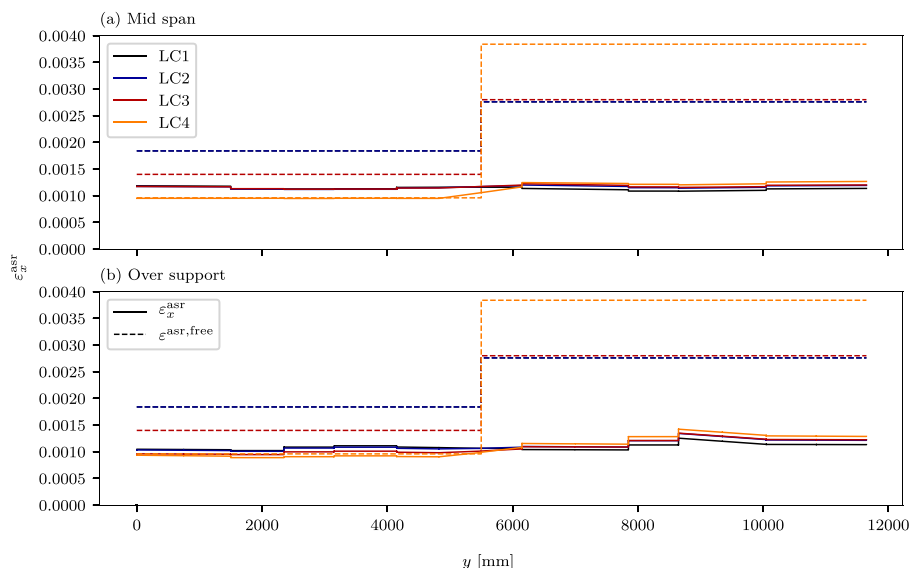
(a) Mid span

(b) Over support

Fig. 19. Imposed ASR expansion in longitudinal direction (x) at the top of the bridge deck along two paths in span 3: (a) in the middle of the span, and (b) at the support. Dashed lines are the corresponding free ASR expansion ($\varepsilon^{\mathrm{asr,free}}$).
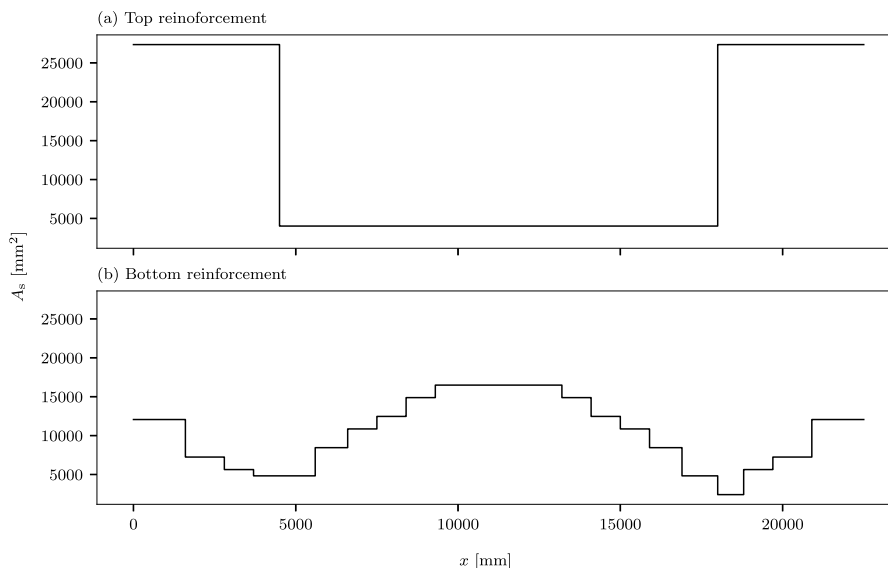

(a) Top reinoforcement

(b) Bottom reinforcement

Fig. 20. Reinforcement distribution in the beams in span 2 to 7; given in total reinforcement area A_s over the beam width of (800 mm).

This method involves solving an inverse problem, which is to calculate the unknown free ASR expansion field from a set of field (in situ) measured displacements, and then use the calculated structural cracks in a final validation step. For practical calculations, an inverse analysis is a reasonable approach to compensate for flaws in the model.

The material model and the structural analysis method were applied on a real case, Elgeseter bridge in Norway. Four different shapes of the free ASR expansion field were investigated, with focus on the ASR-induced stresses.

The following conclusions were drawn from this study:

- The free ASR expansion is a suitable starting point for the modelling of the ASR expansion, especially when used in conjunction with the proposed structural analysis method;
- Even though the free ASR expansion is highly incompatible, i.e. highly non-linear (e.g. strain jumps), the imposed ASR expansion adapts to a strain field that gives less stresses. The ability to adapt

is controlled by the sensitivity of ASR expansion to compressive stress;
- Consequently, the influence of stress on the imposed ASR expansion is of great importance for accurate predictions of the ASR-induced stresses. Further studies on the effect of restraint on expansion are highly supported, especially by use of large scale specimens;
- With the instantaneous stress-expansion relationship W used in this work, the four alternative free ASR expansion fields resulted in differences in stresses that were significant to cause differences in cracking behaviour. Based on the cracking behaviour, we could falsify two of the alternative expansion fields.

The results in this study were obtained based on an ASR expansion model that treats each principal stress directions independently. Further studies on the importance of including the directional coupling (in the expansion model) when analysing similar structures are recommended.
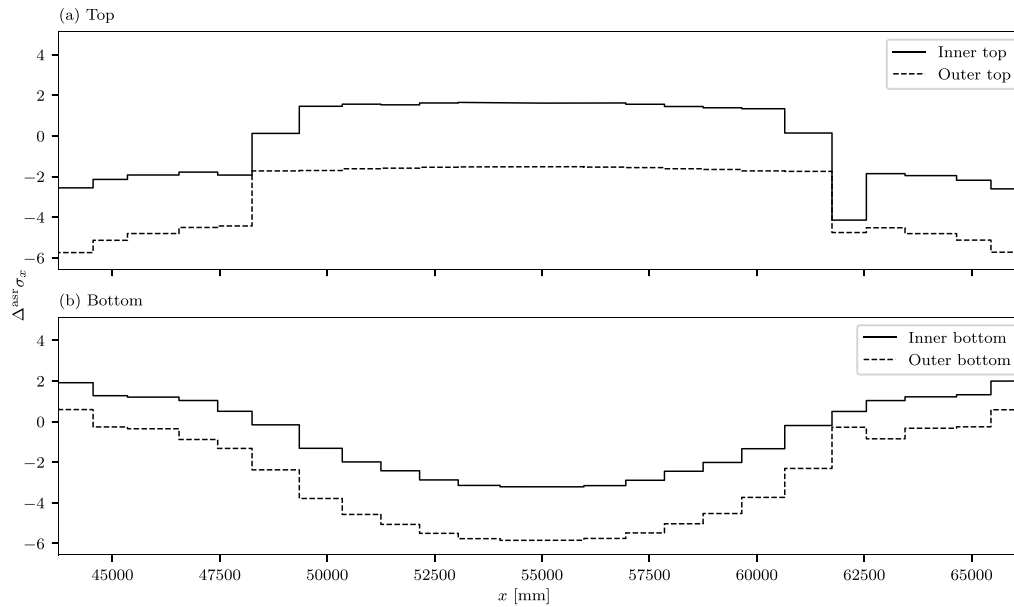
Fig. 21. LC 4. ASR-induced stress (in MPa) in the concrete at the top and the bottom of the beams in span 3.
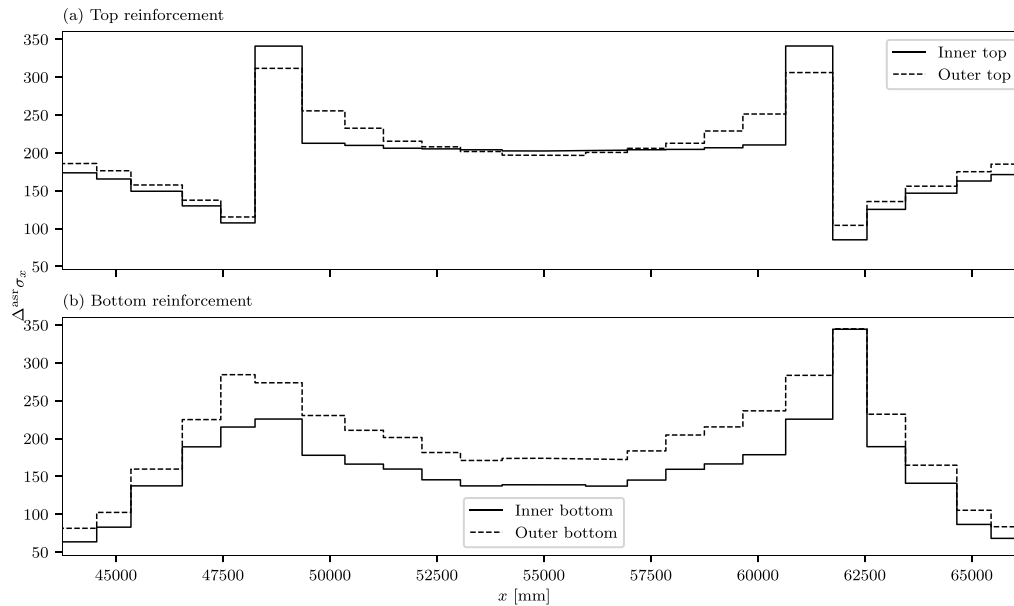

Fig. 22. LC 4. ASR-induced stress (in MPa) at the top and bottom reinforcement in the beams in span 3.

Finally, it is encouraged to further develop an assessment method that merges multiple information on displacement, moisture, temperature, expansion and material properties, in which the information can be used in three ways: (a) as the main observable in the inverse problem (the displacement measurements in this study), (b) as part of the choice of the solution space of the causal variable, or (c) as the part of the validation step (the cracking in this work).

CRediT authorship contribution statement

Simen Sørgaard Kongshaug: Conceptualization, Methodology, Software, Formal analysis, Writing – original draft, Investigation, Writing – review & editing, Visualization. **Max A.N. Hendriks:** Conceptualization, Methodology, Writing – review & editing, Supervision. **Terje Kanstad:** Conceptualization, Methodology, Writing – review & editing, Supervision. **Gro Markeset:** Conceptualization, Methodology, Writing – review & editing, Supervision.

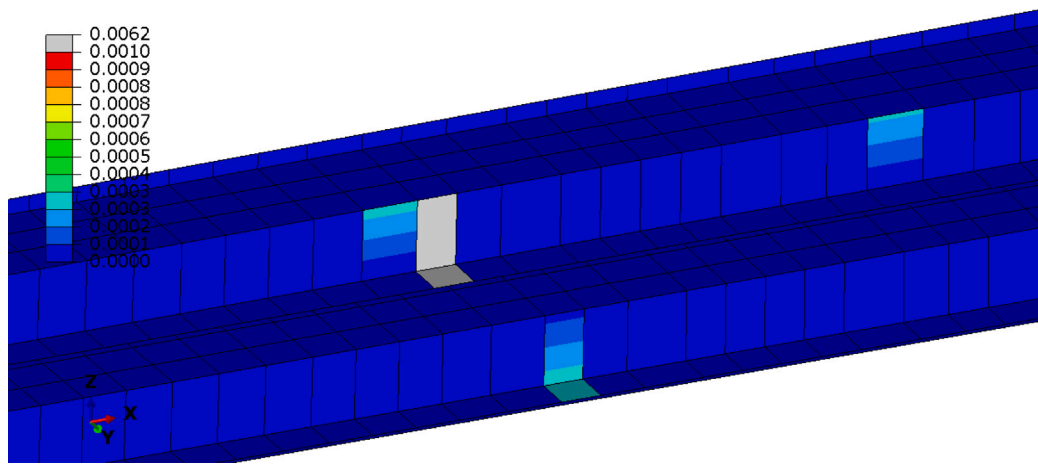**Declaration of competing interest**

The authors declare that they have no known competing financial interests or personal relationships that could have appeared to influence the work reported in this paper.
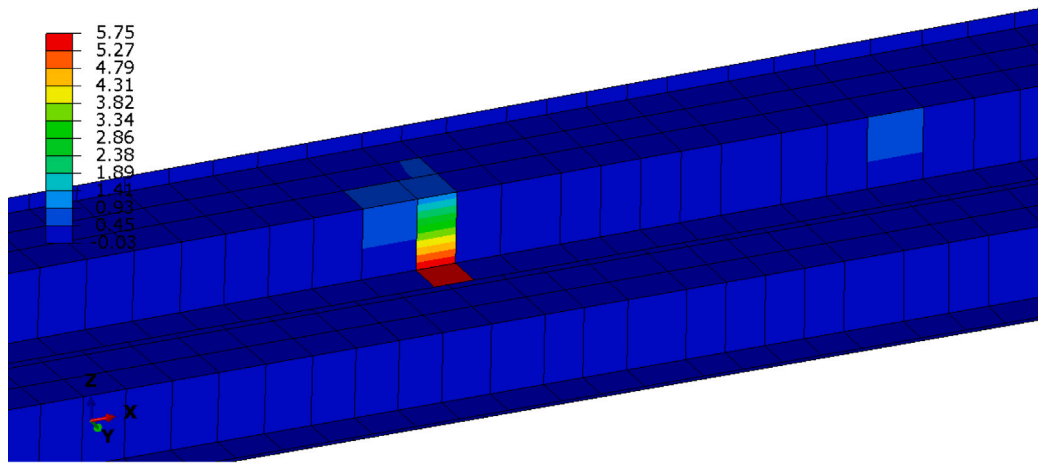
(a) Crack width.

(b) Plastic strain.

Fig. 23. LC 4. 3D view from beneath, where the largest crack occur. The crack width (in mm) is plotted in (a), and the reinforcement plastic strain in (b). The thickness of the shell elements is rendered. The colour scale in (b) is set to a relatively small upper limit of 0.001 to show that plasticity (in the reinforcing bar) at a location where there is no crack. (For interpretation of the references to colour in this figure legend, the reader is referred to the web version of this article.)

Appendix. Solution procedure for the inverse problem

The conditions for minimum of s—the solution of (28)—are

$$\frac{\partial s}{\partial \beta_j} = 0 \quad \text{for} \quad j = 1, 2, \dots, n \tag{A.1}$$

When Eq. (27) is inserted into the minimum conditions (A.1), one achieve the following

$$-2 \sum_{i=1}^{m} (d_i^{\text{obs}} - a_{ik}^{\text{obs}} d_k) a_{il}^{\text{obs}} \frac{\partial d_l}{\partial \beta_j} = 0 \quad \text{(sum over } k \text{ and } l\text{)}$$

$$\Rightarrow \quad \boldsymbol{J}^{\mathrm{T}} \boldsymbol{r} = \boldsymbol{0}; \tag{A.2}$$

$$J_{ij} = a_{il}^{\text{obs}} \frac{\partial d_l}{\partial \beta_j} \quad \text{(sum over } l\text{)}$$

$$r_i = d_i^{\text{obs}} - a_{ik}^{\text{obs}} d_k \quad \text{(sum over } k\text{)}$$

The structural displacement vector $\boldsymbol{d}$ is non-linear in $\boldsymbol{\beta}$, and Eq. (A.2) is solved with the Gauss–Newton method. The initial guess on the vector of parameters is $_0\boldsymbol{\beta}$, and it is updated iteratively by

$$_{n+1}\boldsymbol{\beta} = {}_n\boldsymbol{\beta} + \delta\boldsymbol{\beta};$$

$$\delta\boldsymbol{\beta} = \left[\boldsymbol{J}^{\mathrm{T}} \boldsymbol{J}\right]^{-1} \boldsymbol{J}^{\mathrm{T}} \boldsymbol{r}. \tag{A.3}$$

The expression for $\delta\boldsymbol{\beta}$ is found from the setting the first order Taylor expansion of the left hand side of Eq. (A.2) to the zero vector:

$$\boldsymbol{J}^{\mathrm{T}} \boldsymbol{r} + \frac{\partial (\boldsymbol{J}^{\mathrm{T}} \boldsymbol{r})}{\partial \boldsymbol{\beta}} \delta\boldsymbol{\beta} = \boldsymbol{0}$$

$$\boldsymbol{J}^{\mathrm{T}} \boldsymbol{r} + \left(\frac{\partial \boldsymbol{J}^{\mathrm{T}}}{\partial \boldsymbol{\beta}} \boldsymbol{r} + \boldsymbol{J}^{\mathrm{T}} \frac{\partial \boldsymbol{r}}{\partial \boldsymbol{\beta}} \right) \delta\boldsymbol{\beta} = \boldsymbol{0} \tag{A.4}$$

In the Gauss–Newton method, the expression in the parenthesis (second line of Eq. (A.4)) is approximated by neglecting the first term, which involves second order derivatives of $\boldsymbol{\beta}$. Recognizing that $\frac{\partial \boldsymbol{r}}{\partial \boldsymbol{\beta}} = -\boldsymbol{J}$, and then solve with respect to $\delta\boldsymbol{\beta}$ one achieves the second line of Eq. (A.3).

The matrix $\boldsymbol{J}$ needs some more elaboration, as it involves partial derivative of the displacements (at time t_{end}) $\boldsymbol{d}$ with respect to $\boldsymbol{\beta}$. To find $\boldsymbol{J}$, we need the numerical solution used to calculate $\boldsymbol{d}$. The displacements $\boldsymbol{d}$ are calculated with non-linear FEM with an incremental iterative solution procedure, i.e. for each increment in time, Newton–Raphson iterations in the corresponding increment of displacements are invoked to achieve a state close enough to equilibrium (converged state). The closeness/error to equilibrium is expressed in terms of an out of balance force vector $\boldsymbol{g}$ between external nodal forces $\boldsymbol{R}_{\text{ext}}$ and internal nodal forces $\boldsymbol{R}_{\text{int}}$, given by

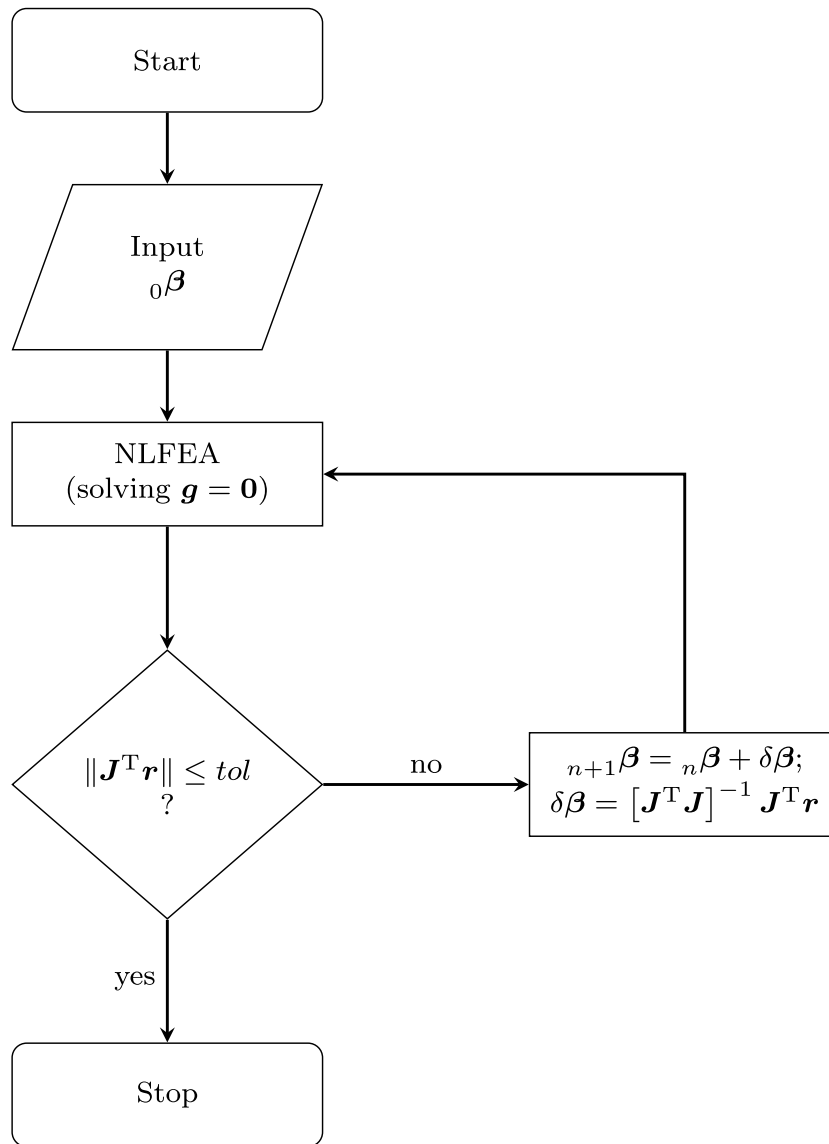$$\boldsymbol{g} = \boldsymbol{R}_{\text{ext}} - \boldsymbol{R}_{\text{int}}, \tag{A.5}$$

Fig. A.24. Flowchart of the solution procedure for the inverse structural ASR problem; iterative non-linear finite element analysis (NLFEA) where β is updated for each analysis until the residual is less than a tolerance value *tol*.

where $g = 0$ is a state of equilibrium. At the final time t_{end}, we assume that equilibrium is achieved. The change in the out of balance force vector due to a small change in the parameters $\delta\beta$ and a small change in displacements δd is approximated by a first order Taylor expansion:

$$g(\beta + \delta\beta, d + \delta d) = g(\beta, d) + \frac{\partial g}{\partial \beta}\delta\beta + \frac{\partial g}{\partial d}\delta d. \tag{A.6}$$

Recognizing that the first term on the right hand side is the zero vector, and by setting the whole expression equal the zero vector to require equilibrium, we achieve

$$\frac{\partial g}{\partial \beta}\delta\beta + \frac{\partial g}{\partial d}\delta d = 0. \tag{A.7}$$

The structural tangent stiffness matrix K can be identified in the second term. The equation is then solved with respect to the displacements:

$$\delta d = K^{-1}\frac{\partial g}{\partial \beta}\delta\beta \tag{A.8}$$

The partial derivative of the displacement with respect to the parameters can now be identified as

$$\frac{\partial d}{\partial \beta} = K^{-1}\frac{\partial g}{\partial \beta}. \tag{A.9}$$

The last step in the elaboration of J is to find the expression for the partial derivative of the out of balance force vector with respect to the parameters (β):

$$\frac{\partial g}{\partial \beta} = -\frac{\partial R_{int}}{\partial \beta} = -\int_V B^{\mathrm{T}}\frac{\partial \sigma}{\partial \beta}\,\mathrm{d}V \tag{A.10}$$

where B is the unit displacement strain matrix. For the ease of reading, the additive split of the integration over the domain V (summation over each finite element) is not expressed in the above equation. Notice that it is only the internal nodal force vector that depends on β. To find the partial derivative of the stress σ with respect to the β, we need an expression for the stress. Combining Eqs. (1), (2) and (7) gives:

$$\sigma = \underbrace{(1 - \omega_{\mathrm{c}})\left[C^{\sigma}\right]^{-1}}_{D_s}(\varepsilon - \varepsilon^{\mathrm{asr}} - \varepsilon^{\mathrm{creep}}) \tag{A.11}$$

In the partial derivative with respect to β, we neglect that the secant stiffness D_{s} depends on β. Including Eqs. (3) and (26), and noticing that the derivative is taken at $t = t_{\text{end}}$, one achieves

$$\frac{\partial \sigma}{\partial \beta} = -D_{\mathrm{s}}\frac{\partial \varepsilon^{\mathrm{asr}}}{\partial \beta} = -D_{\mathrm{s}}W\psi^{\mathrm{T}} \tag{A.12}$$

The final expression for $\boldsymbol{J}$ is found by inserting Eqs. (A.9), (A.10) and (A.12) into Eq. (A.2), which gives

$$\boldsymbol{J} = a^{\mathrm{obs}} \boldsymbol{K}^{-1} \int_V \boldsymbol{B}^{\mathrm{T}} \boldsymbol{D}_{\mathrm{s}} \boldsymbol{W} \boldsymbol{\psi}^{\mathrm{T}} \, \mathrm{d}V \tag{A.13}$$

The solution procedure is illustrated in the flowchart in Fig. A.24.

References

[1] Swamy R, Al-Asali M. Engineering properties of concrete affected by alkali-silica reaction. Mater J 1988;85(5):367–74.

[2] Larive C. Apports combinés de l'expérimentation et de la modélisation à la compréhension de l'alcali-réaction et de ses effets mécaniques (Ph.D. thesis), Ecole nationale des ponts et chaussees; 1997.

[3] Giaccio G, Zerbino R, Ponce J, Batic OR. Mechanical behavior of concretes damaged by alkali-silica reaction. Cem Concr Res 2008;38(7):993–1004.

[4] Esposito R, Anaç C, Hendriks MA, Çopuroğlu O. Influence of the alkali-silica reaction on the mechanical degradation of concrete. J Mater Civ Eng 2016;28(6):04016007.

[5] Jensen V. Alkali–silica reaction damage to Elgeseter Bridge, Trondheim, Norway: a review of construction, research and repair up to 2003. Mater Charact 2004;53(2):155–70. http://dx.doi.org/10.1016/j.matchar.2004.09.006, URL https://www.sciencedirect.com/science/article/pii/S1044580304002086 EMABM 2003: 9th Euroseminar on Microscopy Applied to Building Materials.

[6] Kongshaug SS, Larssen RM, Hendriks MA, Kanstad T, Markeset G. Load effects in reinforced concrete beam bridges affected by alkali–silica reaction—Constitutive modelling including expansion, cracking, creep and crushing. Eng Struct 2021;245:112945. http://dx.doi.org/10.1016/j.engstruct.2021.112945, URL https://www.sciencedirect.com/science/article/pii/S0141029621010890.

[7] Esposito R, Hendriks M. Literature review of modelling approaches for ASR in concrete: a new perspective. Eur J Environ Civ Eng 2017;1–21.

[8] Van Zijl G, De Borst R, Rots J. A numerical model for the time-dependent cracking of cementitious materials. Internat J Numer Methods Engrg 2001;52(7):637–54.

[9] Van Zijl G, De Borst R, Rots J. The role of crack rate dependence in the long-term behaviour of cementitious materials. Int J Solids Struct 2001;38(30–31):5063–79.

[10] Wen HX. Prediction of structural effects in concrete affected by alkali-aggregate reaction (Ph.D. thesis), University of Plymouth; 1993.

[11] Charlwood R, Solymar S, Curtis D. A review of alkali aggregate reactions in hydroelectric plants and dams. In: Proceedings of the international conference of alkali-aggregate reactions in hydroelectric plants and dams, 1992.

[12] Multon S, Toutlemonde F. Effect of applied stresses on alkali–silica reaction-induced expansions. Cem Concr Res 2006;36(5):912–20.

[13] Gautam B, Panesar D, Sheikh S, Vecchio F. Effect of multiaxial stresses on alkali-silica reaction damage of concrete. Materials 2017;114:595–604.

[14] Hayes NW, Gui Q, Abd-Elssamd A, Le Pape Y, Giorla AB, Le Pape S, Giannini ER, Ma ZJ. Monitoring alkali-silica reaction significance in nuclear concrete structural members. J Adv Concr Technol 2018;16(4):179–90.

[15] Berra M, Faggiani G, Mangialardi T, Paolini A. Influence of stress restraint on the expansive behaviour of concrete affected by alkali-silica reaction. Cem Concr Res 2010;40(9):1403–9. http://dx.doi.org/10.1016/j.cemconres.2010.05.002, URL https://www.sciencedirect.com/science/article/pii/S0008884610001213.

[16] Kagimoto H, Yasuda Y, Kawamura M. ASR Expansion, expansive pressure and cracking in concrete prisms under various degrees of restraint. Cem Concr Res 2014;59:1–15.

[17] Liaudat J, Carol I, López CM, Saouma VE. ASR Expansions in concrete under triaxial confinement. Cem Concr Compos 2018;86:160–70.

[18] Jones A, Clark L. The effects of restraint on ASR expansion of reinforced concrete. Mag Concr Res 1996;48(174):1–13.

[19] Gravel C, Ballivy G, Khayat K, Quirion M, Lachemi M. Expansion of AAR concrete under triaxial stresses: Simulation with instrumented concrete block. In: Proc. 11th int. conf. aar, Quebec, Canada, 2000, p. 949–58.

[20] Ahmed TMA, Burley E, Rigden SR. The effect of alkali—silica reaction on the fatigue behaviour of plain concrete tested in compression, indirect tension and flexure. Mag Concr Res 1999;51(6):375–90. http://dx.doi.org/10.1680/macr.1999.51.6.375, arXiv:https://doi.org/10.1680/macr.1999.51.6.375.

[21] Dunant CF, Scrivener KL. Effects of uniaxial stress on alkali–silica reaction induced expansion of concrete. Cem Concr Res 2012;42(3):567–76. http://dx.doi.org/10.1016/j.cemconres.2011.12.004, URL https://www.sciencedirect.com/science/article/pii/S0008884611003267.

[22] Capra B, Sellier A. Orthotropic modelling of alkali-aggregate reaction in concrete structures: numerical simulations. Mech Mater 2003.

[23] Grimal E, Sellier A, Le Pape Y, Bourdarot E. Creep, shrinkage, and anisotropic damage in alkali-aggregate reaction swelling mechanism-Part I: A constitutive model. Mater J 2008;105(3):227–35.

[24] Morenon P, Multon S, Sellier A, Grimal E, Hamon F, Bourdarot E. Impact of stresses and restraints on ASR expansion. Constr Build Mater 2017;140:58–74.

[25] Pourbehi MS, van Zijl GP, et al. Analysis of combined action of seismic loads and alkali-silica reaction in concrete dams considering the key chemical-physical-mechanical factors and fluid-structure interaction. Eng Struct 2019;195:263–73.

[26] Kongshaug SS, Oseland O, Kanstad T, Hendriks MA, Rodum E, Markeset G. Experimental investigation of ASR-affected concrete–the influence of uniaxial loading on the evolution of mechanical properties, expansion and damage indices. Constr Build Mater 2020;245:118384.

[27] Bažant ZP, Oh BH. Crack band theory for fracture of concrete. Matér Constr 1983;16(3):155–77.

[28] Červenka J, Červenka V, Laserna S. On crack band model in finite element analysis of concrete fracture in engineering practice. Eng Fract Mech 2018;197:27–47.

[29] Oliver J. A consistent characteristic length for smeared cracking models. Internat J Numer Methods Engrg 1989;28(2):461–74.

[30] Govindjee S, Kay GJ, Simo JC. Anisotropic modelling and numerical simulation of brittle damage in concrete. Internat J Numer Methods Engrg 1995;38(21):3611–33.

[31] Slobbe A, Hendriks M, Rots J. Systematic assessment of directional mesh bias with periodic boundary conditions: Applied to the crack band model. Eng Fract Mech 2013;109:186–208.

[32] ervenka J, Papanikolaou VK. Three dimensional combined fracture–plastic material model for concrete. Int J Plast 2008;24(12):2192–220. http://dx.doi.org/10.1016/j.ijplas.2008.01.004, URL https://www.sciencedirect.com/science/article/pii/S0749641908000259.

[33] Hordijk DA. Local approach to fatigue of concrete (Ph.D. thesis), 1991.

[34] Stramandinoli RS, La Rovere HL. An efficient tension-stiffening model for nonlinear analysis of reinforced concrete members. Eng Struct 2008;30(7):2069–80.

[35] Smaoui N, Bissonnette B, Bérubé M-A, Fournier B, Durand B. Mechanical properties of ASR-affected concrete containing fine or coarse reactive aggregates. J ASTM Int 2005;3(3):1–16.

[36] Eurocode 2: Design of concrete structures. Part 1-1: General rules and rules for buildings (EN 1992-1-1:2004). CEN European Committee for Standardization; 2004.

[37] Cervenka J, Cervenka V, Eligehausen R. Fracture-plastic material model for concrete, application to analysis of powder actuated anchors. In: Proceedings of the 3rd international conference on fracture mechanics of concrete structures, 1998, pp. 1107–1116.

[38] Østmoen T. Elgeseter bridge – Report from special survey in 2012 (in Norwegian). Tech. rep., Dr. Ing. A. Aas-Jakobsen AS; 2013, URL https://www.mercell.com/sv-se/m/file/GetFile.ashx?id=43152040&version=1.

[39] Larssen RM. Elgeseter bridge – statical classification and strengthening (in norwegian). Tech. rep., Dr. Ing. A. Aas-Jakobsen AS; 2014.

[40] Stemland H, Rodum E, Johansen H. ASR – Guidance for structural analysis (in Norwegian). Tech. rep. 601, Norwegian Public Roads Administration; 2016.

[41] Rodum E, Pedersen BM, Relling RH. Field and laboratory examinations of an ASR-affected bridge–variation in crack extent and water content. In: Proceedings of the 15th ICAAR conference, Sao Paulo, Brazil, 2016.

[42] NS 3473:2003 Concrete structures - Design and detailing rules (in Norwegian). Standards Norway; 2003.